Check for updates

International Journal for Numerical and Analytical Methods in Geomechanics

WILEY

RESEARCH ARTICLE

Three-Dimensional Seismic Response Analysis of Tunnels in Layered Media Using Modified Domain Reduction Method

Bhavesh Banjare[1] | Gauri Ranjan Krishna Chand Avatar[2] | Goudappa Ramanagouda Dodagoudar[1]

[1]Computational Geomechanics Laboratory, Department of Civil Engineering, Indian Institute of Technology Madras, Chennai, Tamil Nadu, India | [2]Department of Aerospace Engineering, Indian Institute of Science, Bengaluru, Karnataka, India

Correspondence: Bhavesh Banjare (ce23d035@smail.iitm.ac.in)

Received: 21 November 2024 | **Revised:** 24 May 2025 | **Accepted:** 18 June 2025

Funding: The authors sincerely acknowledge the support provided by the MoE (Ministry of Education, Govt. of India) scholarship for post-graduate researchers.

Keywords: dynamic soil-structure interaction | fault-rupture mechanism | multi-layer modified domain reduction method | numerical analysis | transfer function | von-Mises stress

ABSTRACT

Fault inclination and complex geological soil features significantly impact the seismic response of underground unlined tunnels. Modeling fault rupture mechanisms necessitates spanning the computational domain over several kilometers, thus making the approach computationally inefficient. In this study, an efficient modeling algorithm, named as multi-layer Modified Domain Reduction Method (MDRM), has been proposed to analyze the Soil-Fault-Tunnel (SFT) system in layered soil media. The study has demonstrated the effectiveness of the MDRM for modeling the SFT system in layered soil media, considering the seismic source, wave propagation path, and local site effects for realistic seismic response assessment of the tunnels. The MDRM algorithm is implemented in an open-source finite element package, MASTODON (Multi-hazard Analysis for STOchastic time-DOmaiN phenomena), based on the MOOSE numerical framework. Using the MDRM approach, parametric simulations for four different fault rupture mechanisms and three distinct tunnel cross-sections (all having the same opening area) are being performed to capture the overall seismic response of the tunnels. The results provide insights into the influence of fault inclination angle, surface wave generation, and local site effects on the response. The transfer function profiles for the considered soil layers are contrasted, and their influence on different tunnel cross-sections is investigated. The findings are useful in the efficient and reliable design of underground tunnels in multi-layered media subjected to different fault rupture mechanisms.

1 | Introduction

Tunnels are the essential infrastructure facilities in the mega cities of the world and are used for a wide range of applications. Safety and sensitivity analysis of tunnels to seismic loading is crucial to ensure their continuous functioning and service. A reliable tunnel design needs accurate soil-fault-tunnel system modeling and consideration of appropriate seismic loading. Many researchers [1–3] studied tunnel damage due to earthquakes and found that the primary reason behind the failure was due to fault fracture zones. Dynamic analysis of the soil-fault tunnel system is a complex wave scattering problem due to the reflection, refraction, transmission, and scattering phenomena. In the past earthquakes such as Kanto (1923), Kobe (1995), Chi-Chi (1999), Niigata (2004), Wenchuan (2008), Tohoku-oki (2011), and Kumamoto (2016), the tunnels have experienced minor to significant damages [4–7] and these observed damages give sufficient evidence that the existing practice needs modification for designing these structures in seismically active regions. Owen and Scholl [8] illustrated the three possible deformation modes

© 2025 John Wiley & Sons Ltd.

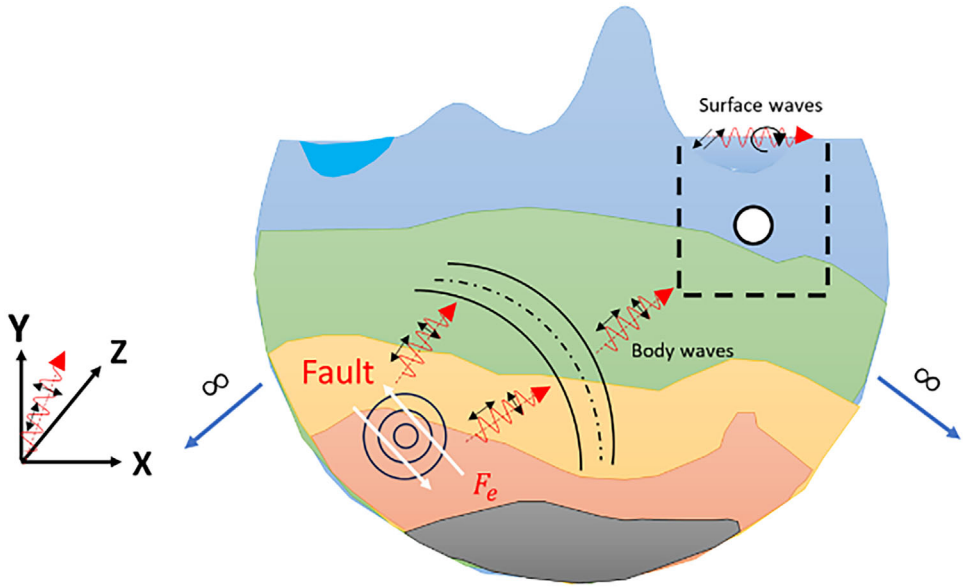


FIGURE 1 | Schematic of soil-fault-tunnel system in semi-infinite half space.

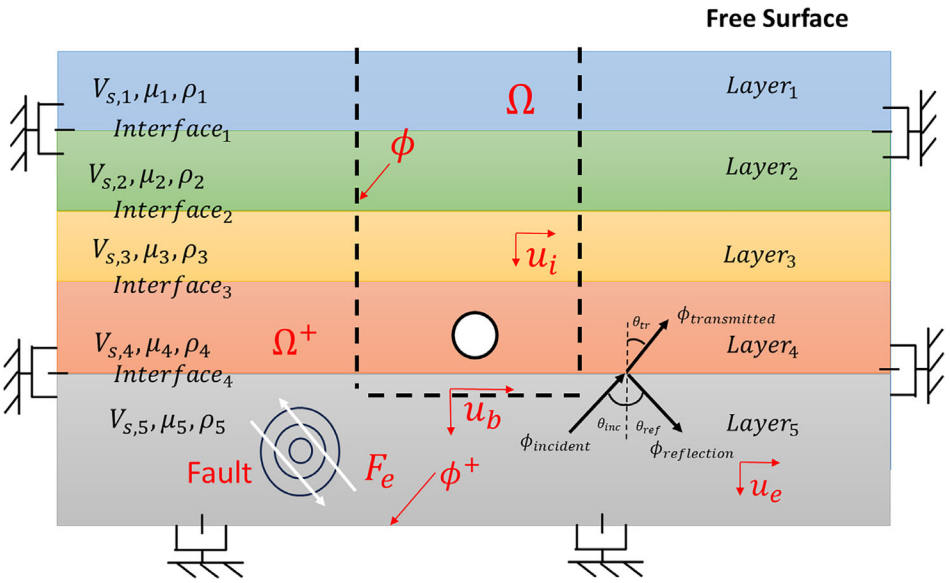


FIGURE 2 | Truncated seismic localized region of interest.

due to seismic loading: i) ovaling deformation, ii) longitudinal bending deformation, and iii) curvature deformation. In near-fault ground motions, the wave fields are quite complex due to the presence of body waves of different incident angles and surface waves (if $\theta_{inc} > \theta_{cr}$; where θ_{inc} is the wave incident angle, and θ_{cr} is the critical incident angle). Corigliano et al. [9] investigated the 2D seismic performance of deep tunnels due to near-fault ground motions using the Domain Reduction Method (DRM). Furthermore, the uncertainties due to the spatial variability of soil properties [10, 11] and ground motions also influence the response of tunnels.

Recently, Garcia-Suarez et al. [12, 13] proposed a 1D analytical approach to deduce the transfer function in layered soil media. Gilbert and Backus [14] demonstrated the propagator matrix method for the evolution of the wave field in layered soil media, which depends on the mechanical properties of the layers. Aki and Richards [15] suggested that the wave field is typically studied using a linear elasticity behavior model, except for soft soils, which require a nonlinear material model [16, 17]. Jahromi et al. [18] developed a partitioned domain decomposition method for solving the coupled nonlinear soil-structure interaction problems. Chen et al. [19] and Chen [20, 21] proposed a finite element method (FEM) based algorithm that utilizes the domain decomposition method to simulate the resistivity of well logging. Ozer et al. [22] developed a finite element shell model for damped multi-layer composite structures based on the principle that the strain energy of a single-layer finite element must be equal to the sum of the strain energies of the individual layers. Zhao et al. [23] introduced an efficient approach for plate structures using constrained layer damping [24] to suppress the vibrations.

10969853, 2025, 13, Downloaded from https://onlinelibrary.wiley.com/doi/10.1002/nag.70006 by The Librarian, Wiley Online Library on [14/08/2025]. See the Terms and Conditions (https://onlinelibrary.wiley.com/terms-and-conditions) on Wiley Online Library for rules of use; OA articles are governed by the applicable Creative Commons License

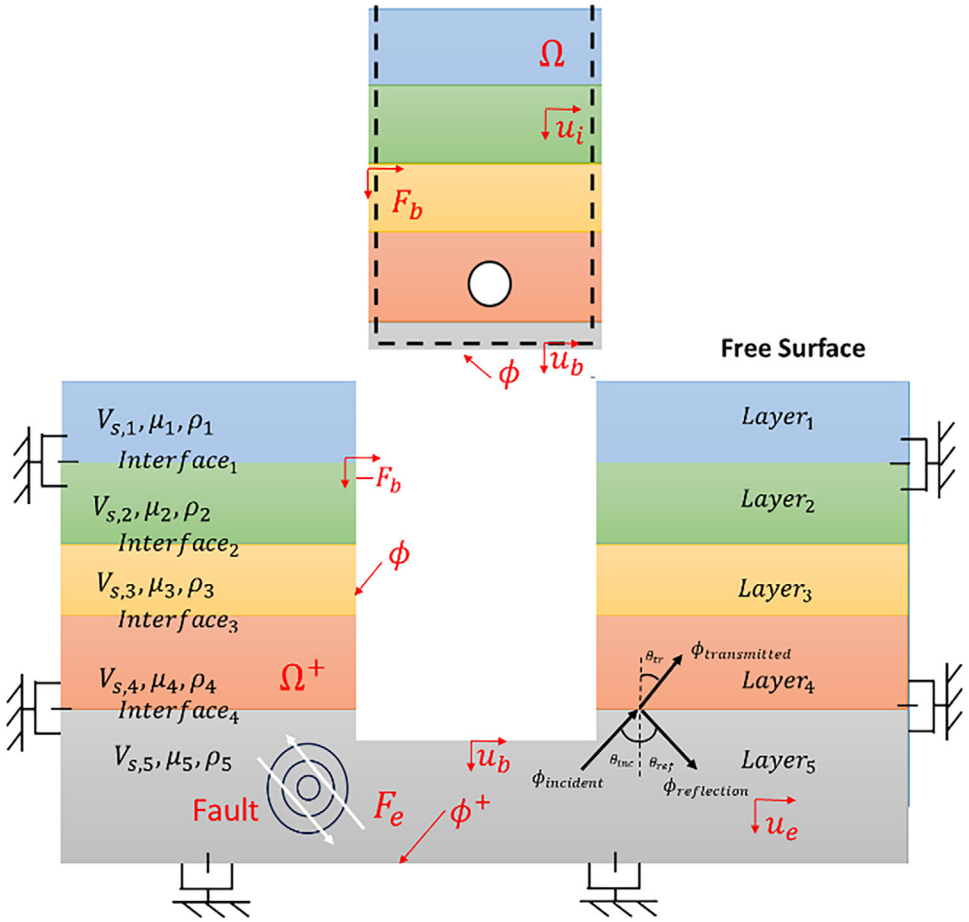


FIGURE 3 | The region of interest is partitioned into two subparts.

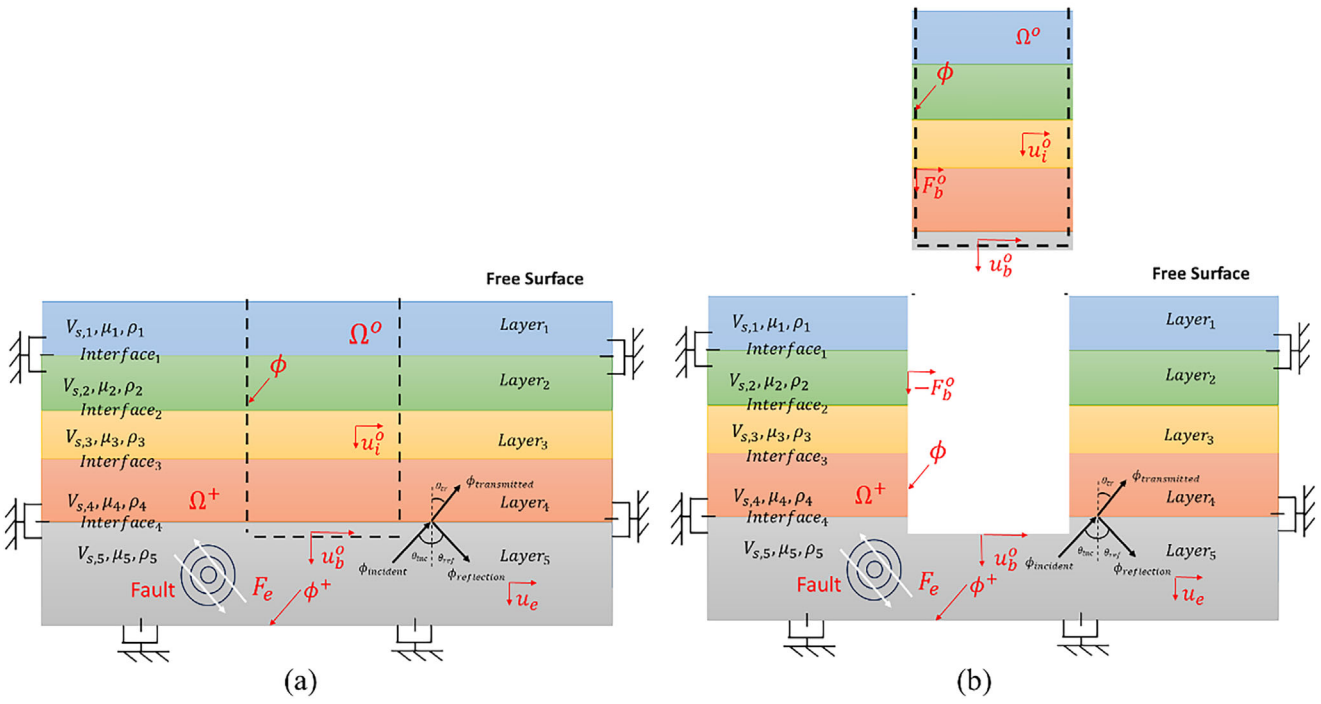


FIGURE 4 | Auxiliary seismic problem (free-field analysis): (a) Region of interest having structure is replaced by an auxiliary domain, and (b) Region is partitioned into two subdomains.

10969853, 2025, 13, Downloaded from https://onlinelibrary.wiley.com/doi/10.1002/nag.70006 by The Librarian, Wiley Online Library on [14/08/2025]. See the Terms and Conditions (https://onlinelibrary.wiley.com/terms-and-conditions) on Wiley Online Library for rules of use; OA articles are governed by the applicable Creative Commons License

Several noteworthy numerical studies have been conducted, such as Li and Song [25] analyzed the tunnel responses under asynchronous ground motion using a viscous-spring boundary for inclined body waves (i.e., P, SV, and SH waves). Huang et al. [26, 27] modeled 2D and 3D finite equivalent nodal forces for obliquely inclined P waves in ABAQUS, and discussed the tunnel responses to different inclination angles. Argyroudis et al. [28] proposed a comprehensive approach for assessing the seismic vulnerability of shallow tunnels, incorporating soil-structure interaction (SSI) and lining degradation due to corrosion employing 2D nonlinear dynamic analyses. Later, Wang et al. [29] extended the DRM using a wave potential formulation (WPF-DRM) to simulate inclined seismic wave effects in horizontally layered media. Their approach enabled the analysis of deeply embedded structures subjected to spatially varying wavefields. Most recently, Korres et al. [30] advanced a weakly coupled Spectral Element Method–Finite Element Method (SEM-FEM) framework that incorporated physics-based earthquake simulations for regional wave propagation into local SSI analysis. Their study focused on optimizing domain size and computational efficiency. Zhang et al. [31] developed a toolbox within the ABAQUS to analyze the rectangular tunnels subjected to obliquely incident SV waves in a uniform soil layer. Zhang and Taciroglu [32] extended this method to 3D time-domain nonlinear analysis of tunnels in layered media. Banjare and Veeraraghavan [33] examined the 2D and 3D responses of underground tunnels under near-fault ground motions and highlighted the significance of wave interactions in assessing the performance of tunnels. Banjare [34] investigated the overall tunnel response to harmonic P- and S- waves for both the shallow [35] and deep tunnels in homogenous strata using the DRM and found that the seismically induced stresses are highly sensitive to tunnel dimensions (i.e., diameter and length) and the wavelength of the incident waves.

Modeling the actual excitation with nodal equivalent forces is proposed by Joyner et al. [36], Lysmer [37], and Lysmer and Kuhlemeyer [38] for one-dimensional wave propagation problems, in which the time history of horizontal nodal force is considered using the dashpots at the base of the soil column domain for incorporating the seismic excitation. Jingbo and Yandong [39] extended this study for inclined waves and multiple support excitation by considering the displacement and stress wave fields are equal to the original ones. Saastamoinen [40] discussed the spectral theory of linear operators for developing the new concept, i.e., "scatter product" for studying the scattering behavior in layered strata. The free-field response analysis in layered media is attempted by Kausel and Ro ̈ esset [41], and they used the Haskell-Thompson transfer matrix for the layered strata, known as the layer stiffness matrix, which is symmetric and minimal operations required for solving the problems involving multi-loading scenarios. Haskell [42] extended the Thomson [43] matrix formulation to find the phase and group velocities of the Rayleigh wave for the layered media. The thin-layer method is proposed by Kausel [44] for dynamic analysis of solids and fluids and has been demonstrated a simple problem of anti-plane impulsive source in homogenous strata. The DRM, an advanced method over the viscous-dashpot models [45] is used for the analysis of seismic wave-field reconstruction in the numerical domain of the wave propagation problem. The DRM is developed by Bielak et al. [46] and Yoshimura et al. [47] for seismic analysis and finite element modeling of large-scale earthquake ground motion problems. This method has been developed to model the realistic seismic ground motion, including body waves (i.e., SH, SV, and P waves) and surface waves (Rayleigh and Love waves). The DRM method is extended for dynamically coupled consolidation problems by Kontoe et al. [48, 49].

Previous numerical studies on response analysis of tunnels have examined the 2D or quasi-3D analyses in simplified homogeneous soil media with unidirectional loading, resulting in less accurate outcomes [9, 10, 27, 50–53]. Veeraraghavan and Banjare [35] introduced a modified Domain Reduction Method designed for analyzing the three-dimensional seismic response of infinitely long tunnels. Their study demonstrated the method's effectiveness through comparisons with semi-analytical solutions [54], addressing tunnel behavior under arbitrary incident seismic waves and emphasizing the significance of domain truncation effects. While their research provided valuable insights into modeling infinitely long tunnels in homogeneous soil conditions, the present study extends this work by focusing on an unlined tunnel embedded in complex horizontally layered media characterized by varying stratigraphy.

Furthermore, our study incorporates fault rupture mechanisms and considers different tunnel cross-sectional geometries to more accurately represent real-world underground systems. The primary objective is to propose a novel MDRM numerical framework for near-fault seismic analysis of tunnels in layered strata. This advanced MDRM framework enhances the traditional DRM by integrating site-specific geological features and surface wave interactions, enabling more realistic simulations of tunnel behavior in fault-affected zones. Finally, this approach aims to improve seismic design and assessment strategies for underground infrastructure in complex geological topography.

The paper is organized as follows. Section 2 presents the MDRM formulation and numerical verification for near-fault scenarios. In Section 3, transfer function formulation for layered media and its influence on bedrock frequency (amplification/attenuation) in the domain is discussed. Section 4 discusses the von Mises stress evolution for different tunnel cross-sections, considering various fault inclinations and tunnel depths. Further, we explain the overall tunnel dynamic response and its causes to prevent this damage/failure. In the end, a summary and conclusion are provided.

2 | Formulation of Multi-Layer Modified Domain Reduction Method

The domain reduction method was initially proposed by Bielak et al. [46] and Yoshimura et al. [47] in 2003. Few studies in the literature have aimed at integrating layered media with underground structure into this framework. This work extends the domain reduction method to accommodate layered media with inclined fault rupture configurations. Figure 1 illustrates the semi-infinite region with complex geological features, including layered media, topography, a seismic source, and structure, where F_e represents the seismic source. The earthquake fault rupture mechanism follows the Huygens–Fresnel principle. According to this principle, every point on a wavefront serves as the source of spherical wavelets, and these secondary wavelets emanate from other points, mutually forming constructive interference

10969853, 2025, 13, Downloaded from https://onlinelibrary.wiley.com/doi/10.1002/nag.70006 by The Librarian, Wiley Online Library on [14/08/2025]. See the Terms and Conditions (https://onlinelibrary.wiley.com/terms-and-conditions) on Wiley Online Library for rules of use; OA articles are governed by the applicable Creative Commons License

in the domain, which generates a new wavefront. The virtual boundary ϕ is defined to separate the semi-infinite region into two segments: Ω and Ω^+. The segment Ω (see Figure 2) encompasses localized features such as the tunnel and topography, while Ω^+ represents the layered media containing the earthquake fault and local site effects. Nodal displacement field for the outer domain Ω^+, boundary ϕ and the interior domain Ω are represented by u_i (internal region), u_b (boundary region), and u_e (external region), respectively. The displacement u_b on the DRM boundary ϕ remains continuous, with F_b denoting the nodal forces transferred from Ω^+ to Ω region (see Figure 3). The ground motion in the domain is governed by Navier's equation of elastodynamics expressed as follows:

$$M_{ij}^{\Omega^l}\ddot{u}_i + C_{ij}^{\Omega^l}\dot{u}_i + K_{ij}^{\Omega^l}\,u_i = F_{ext_i} \tag{1}$$

where $M_{ij}^{\Omega^l}$, $C_{ij}^{\Omega^l}$, $K_{ij}^{\Omega^l}$, and F_{ext_i} denote mass, damping, stiffness, and external force terms, respectively, corresponding to the subdomain Ω^l and superscript index l indicates layer number.

Earthquake ground motion needs to be transferred from the source to the boundary ϕ, an auxiliary problem (see Figure 4) is introduced, replacing the background geological feature with an auxiliary domain. The internal free-field domain is defined as Ω^o, where the localized structure is absent. Boundary forces and nodal displacements are represented as F_b^o, u_b^o, u_i^o, and u_e^o. An intermediate matrix formulation can be derived by adding a damping matrix [C] in the proposed method by Bielak et al. [46]. The equation of motion for reduced domain having localized structure and DRM layer forces is expressed as:

$$\begin{bmatrix} M_{11}^{\Omega^1} & M_{12}^{\Omega^1} & 0 & 0 & 0 & 0 & 0 \\ M_{21}^{\Omega^1} & M_{22}^{\Omega^1}+M_{22}^{\Omega^2} & M_{23}^{\Omega^2} & 0 & 0 & 0 & 0 \\ 0 & M_{32}^{\Omega^2} & M_{33}^{\Omega^2}+M_{33}^{\Omega^3} & M_{34}^{\Omega^3} & 0 & 0 & 0 \\ 0 & 0 & M_{43}^{\Omega^3} & M_{44}^{\Omega^3}+M_{44}^{\Omega^4} & M_{54}^{\Omega^4} & 0 & 0 \\ 0 & 0 & 0 & M_{54}^{\Omega^4} & M_{55}^{\Omega^4}+M_{55}^{\Omega^5} & M_{5b}^{\Omega^5} & 0 \\ 0 & 0 & 0 & 0 & M_{b5}^{\Omega^5} & M_{bb}^{\Omega^5}+M_{bb}^{\Omega^+} & M_{be}^{\Omega^+} \\ 0 & 0 & 0 & 0 & 0 & M_{eb}^{\Omega^+} & M_{ee}^{\Omega^+} \end{bmatrix} \begin{bmatrix} \ddot{u}_1 \\ \ddot{u}_2 \\ \ddot{u}_3 \\ \ddot{u}_4 \\ \ddot{u}_5 \\ \ddot{u}_b \\ \ddot{w}_e \end{bmatrix} +$$

$$\begin{bmatrix} C_{11}^{\Omega^1} & C_{12}^{\Omega^1} & 0 & 0 & 0 & 0 & 0 \\ C_{21}^{\Omega^1} & C_{22}^{\Omega^1}+C_{22}^{\Omega^2} & C_{23}^{\Omega^2} & 0 & 0 & 0 & 0 \\ 0 & C_{32}^{\Omega^2} & C_{33}^{\Omega^2}+C_{33}^{\Omega^3} & C_{34}^{\Omega^3} & 0 & 0 & 0 \\ 0 & 0 & C_{43}^{\Omega^3} & C_{44}^{\Omega^3}+C_{44}^{\Omega^4} & C_{54}^{\Omega^4} & 0 & 0 \\ 0 & 0 & 0 & C_{54}^{\Omega^4} & C_{55}^{\Omega^4}+C_{55}^{\Omega^5} & C_{5b}^{\Omega^5} & 0 \\ 0 & 0 & 0 & 0 & C_{b5}^{\Omega^5} & C_{bb}^{\Omega^5}+C_{bb}^{\Omega^+} & C_{be}^{\Omega^+} \\ 0 & 0 & 0 & 0 & 0 & C_{eb}^{\Omega^+} & C_{ee}^{\Omega^+} \end{bmatrix} \begin{bmatrix} \dot{u}_1 \\ \dot{u}_2 \\ \dot{u}_3 \\ \dot{u}_4 \\ \dot{u}_5 \\ \dot{u}_b \\ \dot{w}_e \end{bmatrix} + \tag{2}$$

$$\begin{bmatrix} K_{11}^{\Omega^1} & K_{12}^{\Omega^1} & 0 & 0 & 0 & 0 & 0 \\ K_{21}^{\Omega^1} & K_{22}^{\Omega^1}+K_{22}^{\Omega^2} & K_{23}^{\Omega^2} & 0 & 0 & 0 & 0 \\ 0 & K_{32}^{\Omega^2} & K_{33}^{\Omega^2}+K_{33}^{\Omega^3} & K_{34}^{\Omega^3} & 0 & 0 & 0 \\ 0 & 0 & K_{43}^{\Omega^3} & K_{44}^{\Omega^3}+K_{44}^{\Omega^4} & K_{54}^{\Omega^4} & 0 & 0 \\ 0 & 0 & 0 & M_{54}^{\Omega^4} & K_{55}^{\Omega^4}+K_{55}^{\Omega^5} & K_{5b}^{\Omega^5} & 0 \\ 0 & 0 & 0 & 0 & K_{b5}^{\Omega^5} & K_{bb}^{\Omega^5}+K_{bb}^{\Omega^+} & K_{be}^{\Omega^+} \\ 0 & 0 & 0 & 0 & 0 & K_{eb}^{\Omega^+} & K_{ee}^{\Omega^+} \end{bmatrix} \begin{bmatrix} u_1 \\ u_2 \\ u_3 \\ u_4 \\ u_5 \\ u_b \\ w_e \end{bmatrix} =$$

$$\begin{bmatrix} 0 \\ 0 \\ 0 \\ 0 \\ 0 \\ -M_{be}^{\Omega^+}\ddot{u}_e^o - C_{be}^{\Omega^+}\dot{u}_e^o - K_{be}^{\Omega^+}u_e^o \\ M_{eb}^{\Omega^+}\ddot{u}_b^o + C_{eb}^{\Omega^+}\dot{u}_b^o + K_{eb}^{\Omega^+}u_b^o \end{bmatrix}$$

10969853, 2025, 13, Downloaded from https://onlinelibrary.wiley.com/doi/10.1002/nag.70006 by The Librarian, Wiley Online Library on [14/08/2025]. See the Terms and Conditions (https://onlinelibrary.wiley.com/terms-and-conditions) on Wiley Online Library for rules of use; OA articles are governed by the applicable Creative Commons License

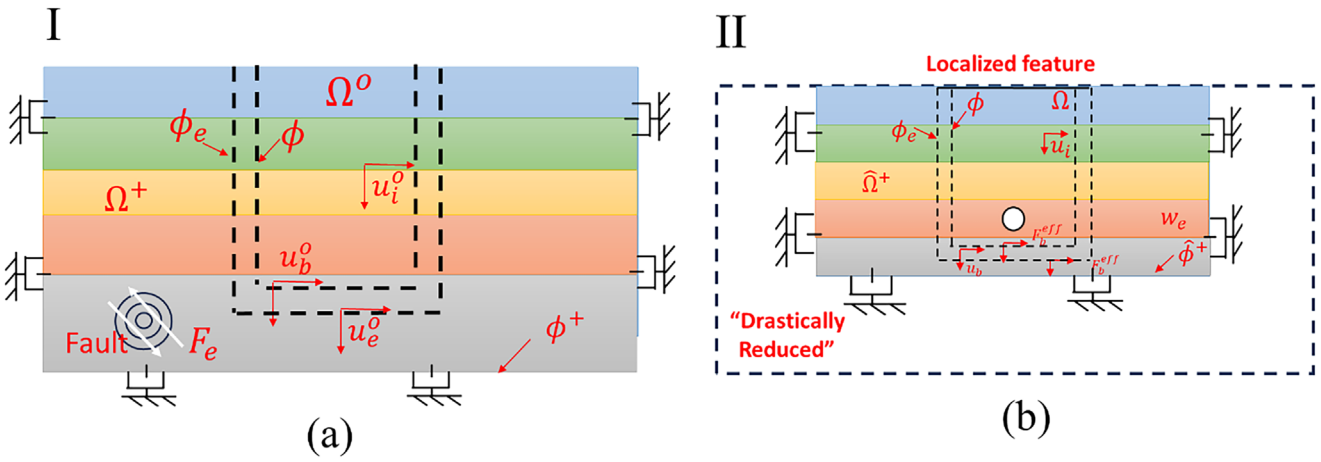


FIGURE 5 | MDRM approach for the combined system. (a) Step I: Free field model considering seismic ground motion and DRM layer force computation, and (b) Step II: Reduced model analysis using DRM layer forces computed in Step I.

The mass matrix (M), damping matrix (C), and stiffness matrix (K) on the left-hand side of Equation (2) are identical to those in Equation (1). Consequently, the seismic force F_e is replaced by the effective nodal forces F_{eff} as shown below:

$$F^{eff} = \begin{bmatrix} F_1^{eff} \\ F_2^{eff} \\ F_3^{eff} \\ F_4^{eff} \\ F_5^{eff} \\ F_b^{eff} \\ F_e^{eff} \end{bmatrix} = \begin{bmatrix} 0 \\ 0 \\ 0 \\ 0 \\ 0 \\ -M_{be}^{\Omega+}\ddot{u}_e^o - C_{be}^{\Omega+}\dot{u}_e^o - K_{be}^{\Omega+}u_e^o \\ M_{eb}^{\Omega+}\ddot{u}_b^o + C_{eb}^{\Omega+}\dot{u}_b^o + K_{eb}^{\Omega+}u_b^o \end{bmatrix} \tag{3}$$

The sub-matrices M_{be}, K_{be}, C_{be} M_{eb}, K_{eb}, and C_{eb} all become zero throughout the domain Ω^+, except for the boundary nodes situated within the ϕ region. Consequently, the computed effective force in the DRM layer of the auxiliary problem is expressed using Equation (3).

The MDRM is a robust two-step algorithm for transferring far-field seismic ground motion to near-field localized regions, as detailed. In the initial step (Figure 5a), we consider a free-field problem comprising the domains Ω_o and Ω^+ to derive the nodal displacement fields u_b^o and u_e^o, which are constrained by the boundaries of layers ϕ and ϕ_e, respectively. In the subsequent step (Figure 5b), we focus on the reduced region defined by $\Omega \cup \hat{\Omega}^+$, encompassing the localized region of interest with the structure. Here, we incorporate the effective nodal forces computed in the first step to determine the unknowns: u_i in Ω region, u_b in ϕ region, and residual displacement field w_e in $\hat{\Omega}^+$ domain.

2.1 | Verification of Multi-Layer Modified Domain Reduction Method With Numerical Problem

The MDRM algorithm is implemented in an open-source finite element package called MASTODON (https://mooseframework.inl.gov/mastodon/), based on the MOOSE numerical framework.

The proposed numerical workflow of MDRM is presented in Figure 6. The moment matrix $M_0(p,t)$ is computed for each point source (p) and each time instant (t) using the *Seismic-Source Block* within the Dirac-Kernel module [55]. The seismic moment $M_0(t)$ of the seismic source is defined as (Equation 4):

$$M_0(t) = GA\bar{s}(\omega, t) \tag{4}$$

where A = area of fault rupture, G = shear modulus of soil, and $\bar{s}(\omega, t)$ = averaged slip-displacement rate of the fault.

The seismic moment $M_0(t)$ is transformed into the global coordinate system (x, y, and z), where the z-axis is oriented along the geographic north, and the y-axis along the soil depth. The resulting moment can be expressed in a symmetric 3 × 3 matrix form [15]. The components of the seismic moment matrix tensor are as follows:

$$M_{xx}(t) = -M_0(t)\left(\sin\delta\cos\lambda\sin 2\phi_s + \sin 2\delta\sin\lambda\, sin^2\phi_s\right) \tag{5}$$

$$M_{xy}(t) = M_0(t)\left(\sin\delta\cos\lambda\cos 2\phi_s + \frac{1}{2}\sin 2\delta\sin\lambda\sin 2\phi_s\right) = M_{yx}(t) \tag{6}$$

$$M_{xz}(t) = -M_0(t)\left(\cos\delta\cos\lambda\cos\phi_s + \cos 2\delta\sin\lambda\sin 2\phi_s\right) = M_{zx}(t) \tag{7}$$

$$M_{yy}(t) = M_0(t)\left(\sin\delta\cos\lambda\sin 2\phi_s - \sin 2\delta\sin\lambda\, cos^2\phi_s\right) \tag{8}$$

$$M_{yz}(t) = -M_0(t)\left(\cos\delta\cos\lambda\sin\phi_s - \cos 2\delta\sin\lambda\cos\phi_s\right) = M_{zy}(t) \tag{9}$$

$$M_{zz}(t) = M_0(t)\left(\sin 2\delta\sin\lambda\right) \tag{10}$$

where ϕ_s is the strike, δ is the dip angle, and λ is the slip direction. Each component of the matrix represents a force couple, where the first index indicates the direction of the force, and the second index specifies the direction in which the forces are separated.

10969853, 2025, 13, Downloaded from https://onlinelibrary.wiley.com/doi/10.1002/nag.70006 by The Librarian, Wiley Online Library on [14/08/2025]. See the Terms and Conditions (https://onlinelibrary.wiley.com/terms-and-conditions) on Wiley Online Library for rules of use; OA articles are governed by the applicable Creative Commons License

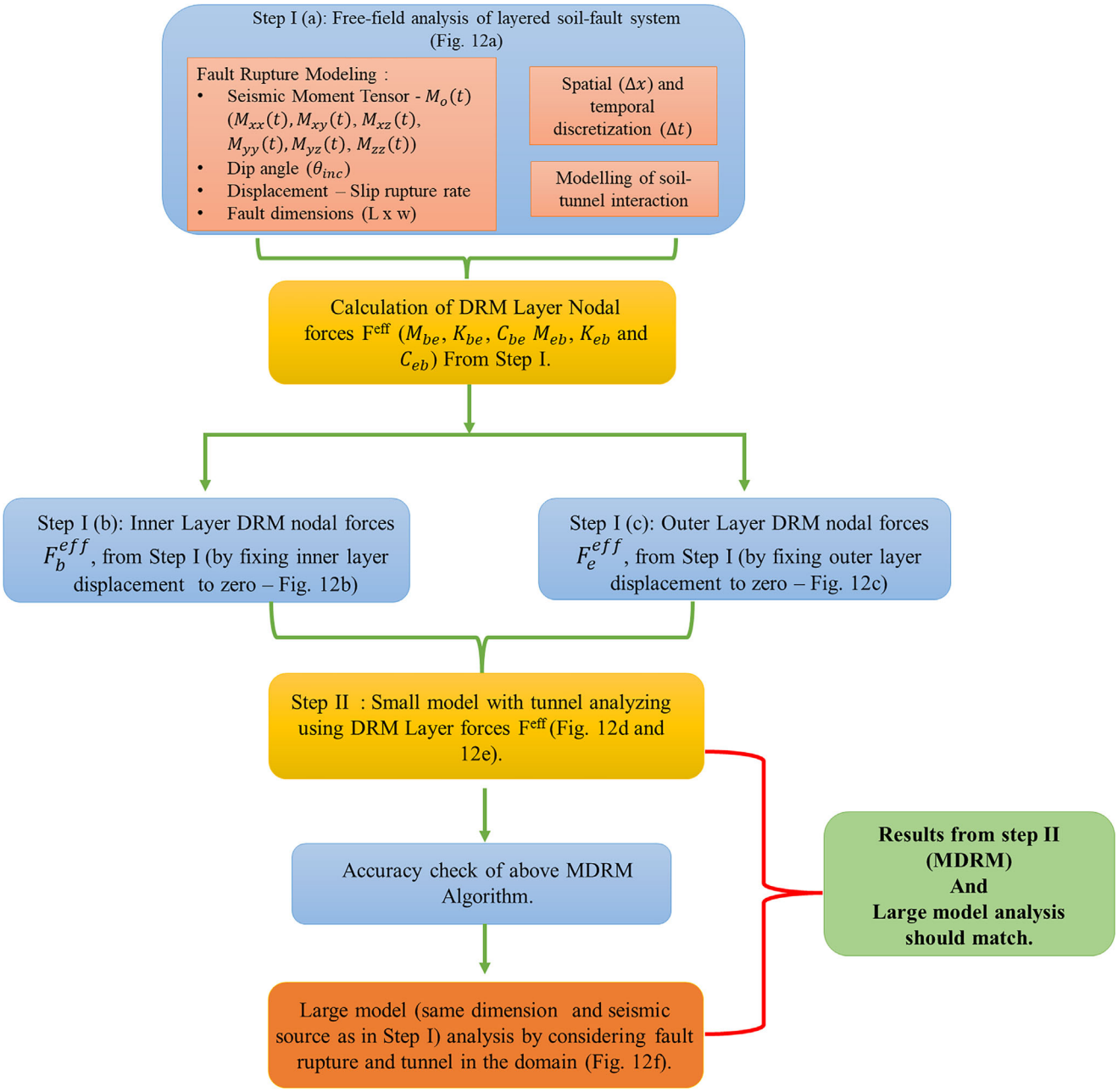


FIGURE 6 | The schematic flow chart of implementing the MDRM algorithm in MASTODON.

Equations (5–10) are used to generate 3D inclined waves in the numerical domain to model an earthquake source.

The slip motion is described using the expression [56] as follows (Equation 11):

$$\bar{s}(\omega,t)=\begin{cases}0, & t<0\\ 1-e^{-\omega t}\left[1+\omega t+\frac{1}{2}(\omega t)^2+\frac{1}{6}(\omega t)^3-\left(\frac{3}{2x_o^2}+\frac{1}{3x_o}\right)(\omega t)^4+\left(\frac{1}{x_o^3}+\frac{1}{6x_o^2}\right)(\omega t)^5\right], & 0\le \omega t\le x_o\\ 1-e^{-\omega t}(1+\omega t), & \omega t>x_o\end{cases} \tag{11}$$

where $x_o = 2.31$, ω is chosen as 6.5 Hz (corner frequency), and t indicates time. The selected corner frequency ensures that ground motions up to 10 Hz contribute significantly. Slip-displacement variation at each point source on the earthquake fault plane is shown in Figure 7.

10969853, 2025, 13, Downloaded from https://onlinelibrary.wiley.com/doi/10.1002/nag.70006 by The Librarian, Wiley Online Library on [14/08/2025]. See the Terms and Conditions (https://onlinelibrary.wiley.com/terms-and-conditions) on Wiley Online Library for rules of use; OA articles are governed by the applicable Creative Commons License

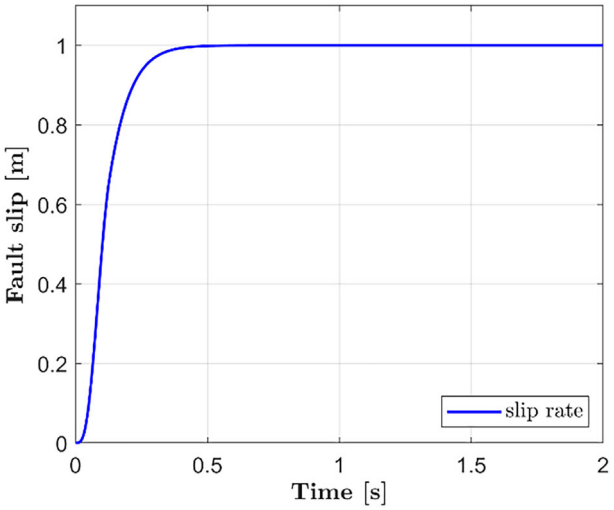


FIGURE 7 | Variation of slip displacement time history at each point source on the earthquake fault plane [11].

TABLE 1 | Seismic source parameters.

Slip direction (δ)	30^o
Slip Direction (λ)	90^o
Strike (ϕ_s)	0^o
Shear Modulus (GPa)	2.194e7
Point sources	16032
Slip rate	Uniform
Fault Dimension (L × W)	520 m × 300 m

A 3D half-space domain with seismic source is considered for free-field analysis as shown in Figure 8. For step I (Outlined in Figure 6), a model dimension of 500 m × 700 m × 1000 m is considered (Figure 9). This study considers 10 nodes per wavelength scheme [57] to determine the optimal mesh size. In the numerical model, the 6-noded prismatic element and 8-noded brick element are considered with finer mesh near the tunnel section (see Figure 10) and coarser mesh in areas further from the structure. The earthquake fault rupture mechanism is modeled by discretizing the fault into the finite number of point sources (Figure 11a–d) in the MASTODON software [55].

The modeling parameters for the seismic fault are outlined in Table 1, and layered media properties are listed in Table 2. Newmark-β time integration approach [58] is employed to compute the velocity and acceleration at each time step, renowned for its effectiveness in implicit time integration. The chosen parameters $\beta = 0.25$ and $\gamma = 0.5$, ensure the method unconditional stability, making it suitable for complex seismic analyses. Viscous absorbing boundaries [38], that is, Lysmer dampers are applied on all boundaries except the top boundary of the model. These boundaries are crucial for dissipating residual seismic waves within the domain, preventing reflection, and ensuring more accurate simulation results. However, viscous boundaries alone might not suffice to absorb all scattered waves. Therefore, Rayleigh damping coefficients η and ζ (see Table 1) are integrated into the model to mitigate these scattered waves further. This damping method is particularly effective in reducing the amplitude of high-frequency waves that are not completely absorbed by the Lysmer dampers at the boundaries. The combination of viscous absorbing boundaries and Rayleigh damping ensures a more comprehensive approach to manage wave propagation and absorption in the model, leading to more precise and reliable simulation outcomes. This setup is crucial for accurately capturing the complex interaction behaviors of seismic waves as they travel through layered geological media.

For Steps I(b) and I(c) (see Figure 6), a single-layer DRM (Figure 8) is modeled for obtaining the effective nodal forces (Equation 10) from Step I(a). To obtain F_b^{eff}, we prescribe zero displacement to inner nodes and calculate the inner node boundary forces from step I(a), the acceleration field is then applied to the outer layer (see Figure 12b). Similarly, we compute F_e^{eff}, and the resultant acceleration field is applied to the inner layer (see Figure 12c).

A reduced 3D model dimension of 150 m × 300 m × 1000 m is considered with an unlined tunnel diameter of 12 m for analysis of Step II (Figure 12d,e). The DRM layer effective nodal forces F^{eff} calculated in Steps I(b) and I(c) are used as a seismic source for Step II (reduced domain) simulation. A preconditioned Jacobian-free Newton-Krylov [59] solver is employed to solve the numerical system, offering improved convergence characteristics. The simulation runs for 2.0 s. The computational time for the large model simulation is 6 h, whereas using the MDRM approach, the time is reduced to approximately 0.77 h.

The acceleration time histories recorded at the locations [X = 250 m, Y = 0 m, Z = 500 m], [X = 250 m, Y = 150 m, Z = 500 m], and [X = 256 m, Y = 200 m, Z = 500 m] are shown in Figure 13. Notably, the outcomes from the large model (Figure 12f) analysis, which involved a comprehensive model encompassing the SFT system, exhibit a remarkable congruence with those from Step II, where a reduced domain (~8 times smaller than big model) with effective nodal forces was applied. This consistency across different simulation scenarios substantiates and affirms the effectiveness of MDRM.

2.2 | Complex Wave Field Due to SV Wave

The SV waves traveling upward interact with the layer interface and free surface (Figure 12a), and the incidence angle of the SV wave determines whether surface waves are generated. The reflected angle of the P-wave is calculated using Snell's law as follows:

$$\frac{sin(\theta_1)}{V_1} = \frac{sin(\theta_2)}{V_2} = \frac{sin(\theta_3)}{V_3} = \frac{sin(\theta_4)}{V_4} = \frac{sin(\theta_5)}{V_5} = constant \quad (12)$$

where θ_i represent the incidence angle or reflected angles at each layer interface, and V_i is the wave velocity in the i_{th} layer. The incidence angle at which the reflected angle becomes 90° is known as the critical incidence angle (θ_c). For soil with a Poisson's ratio of 0.3, the critical incidence angle is 32.23°. The wave field in the domain is complex due to the presence of different types of body and surface waves (see Table 3).

10969853, 2025, 13, Downloaded from https://onlinelibrary.wiley.com/doi/10.1002/nag.70006 by The Librarian, Wiley Online Library on [14/08/2025]. See the Terms and Conditions (https://onlinelibrary.wiley.com/terms-and-conditions) on Wiley Online Library for rules of use; OA articles are governed by the applicable Creative Commons License

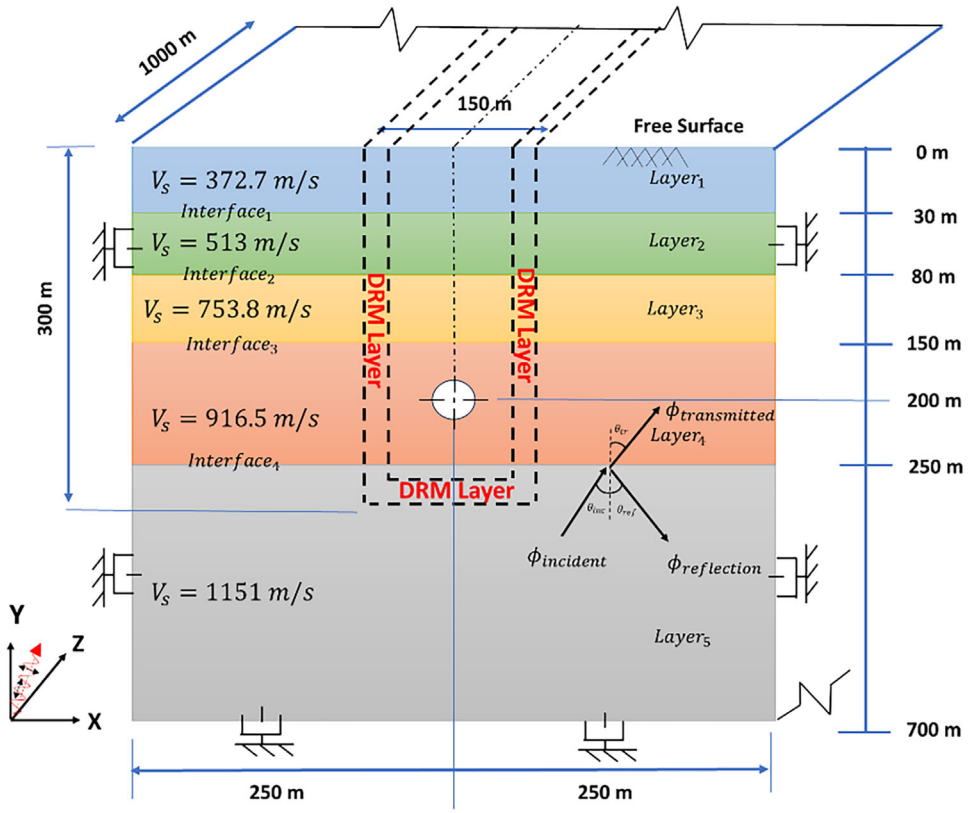


FIGURE 8 | Schematic of the soil-fault-tunnel system considered for numerical analysis.

TABLE 2 | Material parameters.

Layers ID	d (m)	V_s (m/s)	V_p (m/s)	υ	Rayleigh damping coefficient (mass proportional) η	Rayleigh damping coefficient (stiffness proportional) ζ
1	30	372.7	698.81	0.3	0.0014	0.4155
2	50	513	961.87	0.3	0.0010	0.3019
3	70	753.8	1413.37	0.3	6.8707×10^{-4}	0.2054
4	100	916.5	1718.43	0.3	5.6510×10^{-4}	0.1690
5	450	1151	2158.12	0.3	4.4997×10^{-4}	0.1345

TABLE 3 | Different types of body and surface waves in the numerical domain based on fault incidence angle (θ_i).

Fault inclination angle	Incidence angle of SV-wave (θ_i)	Reflected angle of SV-wave (θ_r)	The reflected angle of P-wave (r) $r = sin^{-1}\left(\frac{V_P}{V_s} sin(\theta_i)\right)$	Surface-wave generated or not (critical incidence angle (θ_c) = 32.23°)
30° (Figure 12e)	30°	30°	69.63°	No, $\theta_i < 32.23°$
45° (Figure 14a)	45°	45°	An incidence angle of 45° presents a unique case where all the energy is reflected as SV wave wavefront, resulting in no surface wave generation [33].	
55° (Figure 14b)	55°	55°	No reflected P-wave is produced, as surface waves are generated.	Yes, $\theta_i > 32.23°$ (Rayleigh waves will be generated)
65° (Figure 14c)	65°	65°	No reflected P-wave is produced, as surface waves are generated.	Yes, $\theta_i > 32.23°$ (Rayleigh waves will be generated)

10969853, 2025, 13, Downloaded from https://onlinelibrary.wiley.com/doi/10.1002/nag.70006 by The Librarian, Wiley Online Library on [14/08/2025]. See the Terms and Conditions (https://onlinelibrary.wiley.com/terms-and-conditions) on Wiley Online Library for rules of use; OA articles are governed by the applicable Creative Commons License

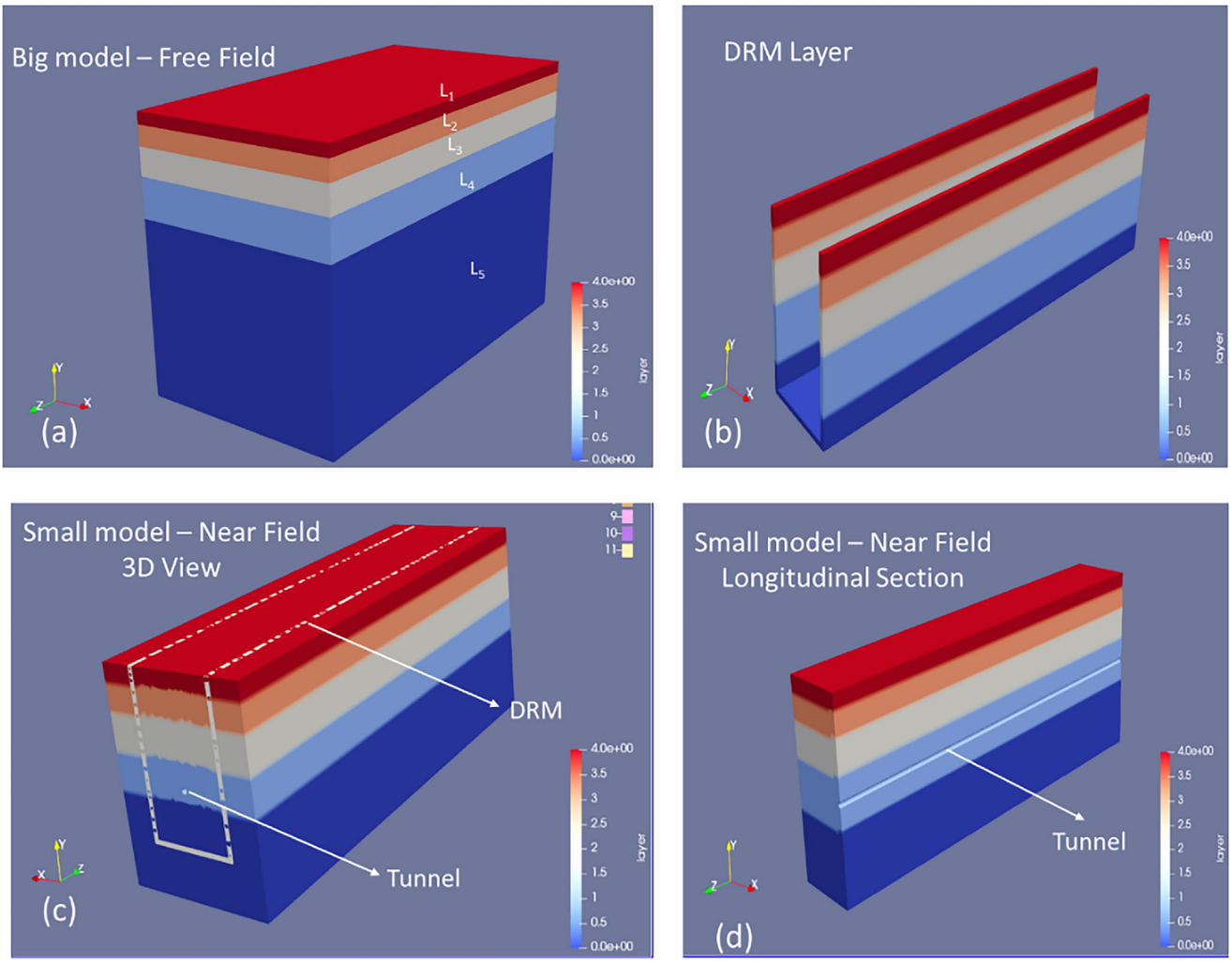


FIGURE 9 | Layered numerical models considered for analysis: (a) Big model, (b) DRM Layer, (c) Small model, and (d) Small model sectional view.

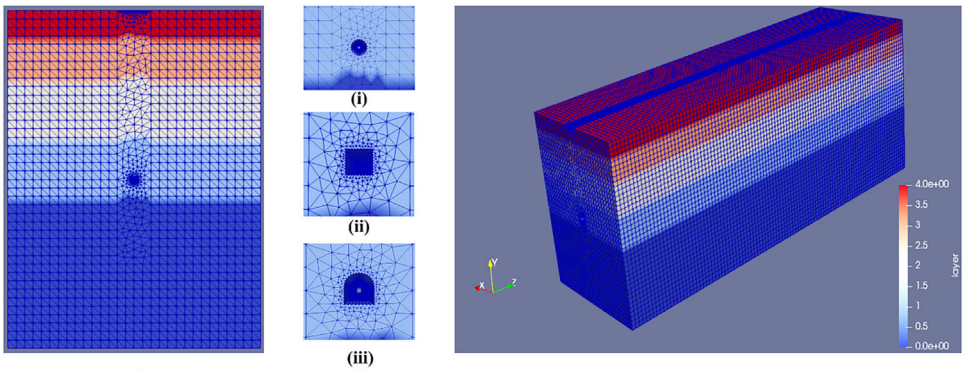


FIGURE 10 | Mesh discretization of the numerical model: (a) Sectional view, (b) Magnified view of the cross-section of the tunnel–(i) Circular, (ii) Square, and (iii) Horseshoe, and (c) Longitudinal View.

3 | Transfer Function for Surface-to-Borehole

The transfer function [60] relates each frequency of input seismic motion to be amplified or deamplified based on soil strata mechanical properties. Since the three-dimensional soil system is finite and has a layered profile, the wave dynamics are complex, undergoing multiple reflections and refractions at the bilayer interfaces. As a result, the construction of transfer functions to determine ground response is done empirically. In order to obtain approximate transfer functions for our problem (*to compare the 3D numerical results*), we consider N soil layers stacked over one another. Each soil layer has a finite thickness but infinite lateral dimensions. Consequently, the wave travels only vertically.

10969853, 2025, 13, Downloaded from https://onlinelibrary.wiley.com/doi/10.1002/nag.70006 by The Librarian, Wiley Online Library on [14/08/2025]. See the Terms and Conditions (https://onlinelibrary.wiley.com/terms-and-conditions) on Wiley Online Library for rules of use; OA articles are governed by the applicable Creative Commons License

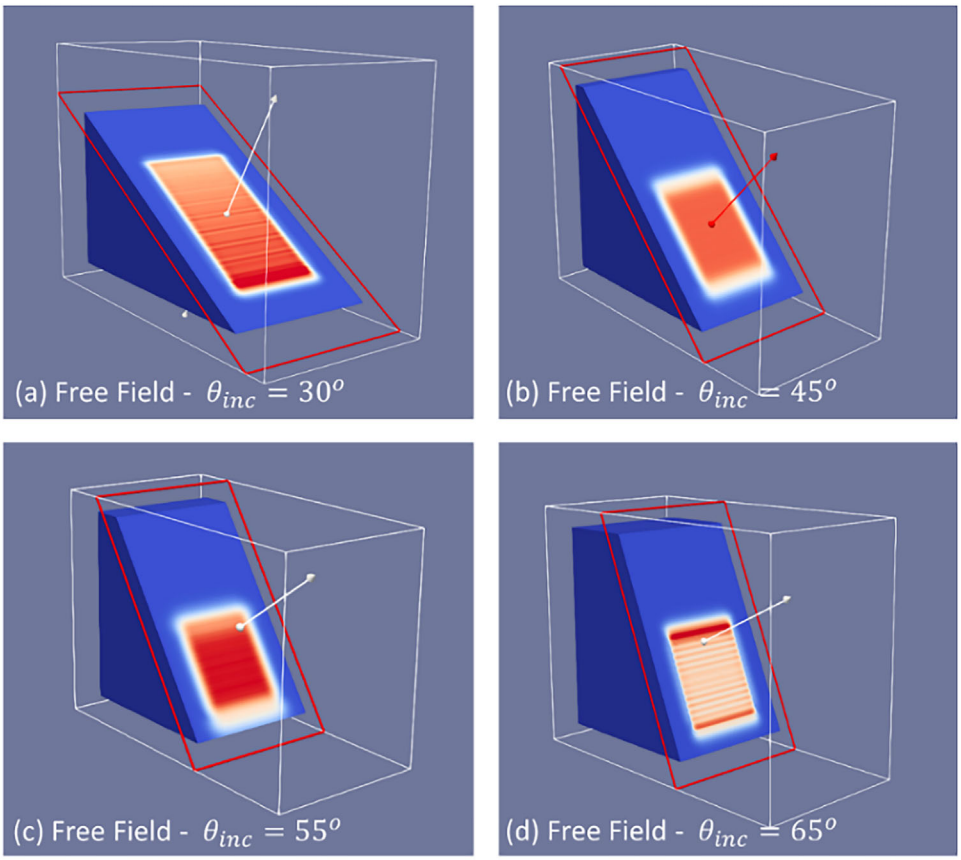


FIGURE 11 | Free-field model with fault inclined at (a) 30°, (b) 45°, (c) 55°, and (d) 65°.

A transfer function is expressed as the ratio of displacement at the free surface (u_{top}) to the bedrock displacement (u_b). Following Kramer [17], the displacement function for layer j is expressed as (Figure 15):

$$U_j(z_j, t) = \left(A_j e^{ik_j^* z_j} + B_j e^{-ik_j^* z_j}\right) e^{i\omega t} \tag{13}$$

where,

$$k_j^* = k(1 - i\xi)$$

$$A_{j+1} = \frac{1}{2}A_j\left(1 + \alpha_j e^{ik_j^* h_j}\right) + \frac{1}{2}B_j\left(1 - \alpha_j e^{-ik_j^* h_j}\right)$$

$$B_{j+1} = \frac{1}{2}A_j\left(1 - \alpha_j e^{ik_j^* h_j}\right) + \frac{1}{2}B_j\left(1 + \alpha_j e^{-ik_j^* h_j}\right)$$

$$TF(\omega)^{-1} = \frac{U_j(0,\ t)}{U_b(H,\ t)} \tag{14}$$

Transfer function relation for N layers is given by Garcia-Suarez et al. [12] and is of the form:

$$\mathrm{T\,F}_{u-u}(\omega)^{-1} = \left(\prod_{i=1}^{N}\cos(r_i)\right)\left(\sum_{\beta=0}^{\lfloor N/2\rfloor}\sum_{|b|=2\beta} C_b \tan(r)^b\right) \tag{15}$$

where $\lfloor . \rfloor$ is the floor function, $r_i = \omega h_i/\sqrt{\mu_i/\rho_i}$, binary multi-index [61] b $\epsilon[0,1]^N$ the coefficients C_b given by $C_b = (-1)^{|b|/2}(\sqrt{\rho\mu})^{f(b)}$. We obtained the expressions of transfer functions for a 5-layer profile using a symbolic package called *Mathematica 13.1*.

Example: $N = 5$ layers

$$\begin{aligned}
&\mathrm{T\,F}_{u-u}(\omega)^{-1} = \cos(\mathrm{r}_1)\cos(\mathrm{r}_2)\cos(\mathrm{r}_3)\cos(\mathrm{r}_4)\cos(\mathrm{r}_5)\\
&\Big\{1 - \sqrt{\tfrac{\rho_1\mu_1}{\rho_2\mu_2}}\tan(\mathrm{r}_1)\tan(\mathrm{r}_2) - \sqrt{\tfrac{\rho_1\mu_1}{\rho_3\mu_3}}\tan(\mathrm{r}_1)\tan(\mathrm{r}_3)\\
&-\sqrt{\tfrac{\rho_1\mu_1}{\rho_4\mu_4}}\tan(\mathrm{r}_1)\tan(\mathrm{r}_4) - \sqrt{\tfrac{\rho_1\mu_1}{\rho_5\mu_5}}\tan(\mathrm{r}_1)\tan(\mathrm{r}_5)\\
&-\sqrt{\tfrac{\rho_2\mu_2}{\rho_3\mu_3}}\tan(\mathrm{r}_2)\tan(\mathrm{r}_3) - \sqrt{\tfrac{\rho_2\mu_2}{\rho_4\mu_4}}\tan(\mathrm{r}_2)\tan(\mathrm{r}_4) - \sqrt{\tfrac{\rho_2\mu_2}{\rho_5\mu_5}}\\
&\tan(\mathrm{r}_2)\tan(\mathrm{r}_5) - \sqrt{\tfrac{\rho_3\mu_3}{\rho_4\mu_4}}\tan(\mathrm{r}_3)\tan(\mathrm{r}_4) - \sqrt{\tfrac{\rho_3\mu_3}{\rho_5\mu_5}}\tan(\mathrm{r}_3)\tan(\mathrm{r}_5)\\
&-\sqrt{\tfrac{\rho_4\mu_4}{\rho_5\mu_5}}\tan(\mathrm{r}_4)\tan(\mathrm{r}_5) + \sqrt{\tfrac{\rho_1\mu_1}{\rho_2\mu_2}}\sqrt{\tfrac{\rho_3\mu_3}{\rho_4\mu_4}}\tan(\mathrm{r}_1)\tan(\mathrm{r}_2)\tan(\mathrm{r}_3)\\
&\tan(\mathrm{r}_4) + \sqrt{\tfrac{\rho_1\mu_1}{\rho_2\mu_2}}\sqrt{\tfrac{\rho_3\mu_3}{\rho_5\mu_5}}\tan(\mathrm{r}_1)\tan(\mathrm{r}_2)\tan(\mathrm{r}_3)\tan(\mathrm{r}_5) +\\
&\sqrt{\tfrac{\rho_1\mu_1}{\rho_2\mu_2}}\sqrt{\tfrac{\rho_4\mu_4}{\rho_5\mu_5}}\tan(r_1)\tan(r_2)\tan(r_4)\tan(r_5) + \sqrt{\tfrac{\rho_1\mu_1}{\rho_3\mu_3}}\\
&\sqrt{\tfrac{\rho_4\mu_4}{\rho_5\mu_5}}\tan(r_1)\tan(r_3)\tan(r_4)\tan(r_5) +\\
&\sqrt{\tfrac{\rho_2\mu_2}{\rho_3\mu_3}}\sqrt{\tfrac{\rho_4\mu_4}{\rho_5\mu_5}}\tan(\mathrm{r}_2)\tan(\mathrm{r}_3)\tan(\mathrm{r}_4)\tan(\mathrm{r}_5)\Big\}
\end{aligned} \tag{16}$$

The analytical form of the free surface to bedrock transfer function proposed by Garcia-Suarez et al. [12] to compute the corresponding transfer function for the N = 5-layer system is

10969853, 2025, 13, Downloaded from https://onlinelibrary.wiley.com/doi/10.1002/nag.70006 by The Librarian, Wiley Online Library on [14/08/2025]. See the Terms and Conditions (https://onlinelibrary.wiley.com/terms-and-conditions) on Wiley Online Library for rules of use; OA articles are governed by the applicable Creative Commons License

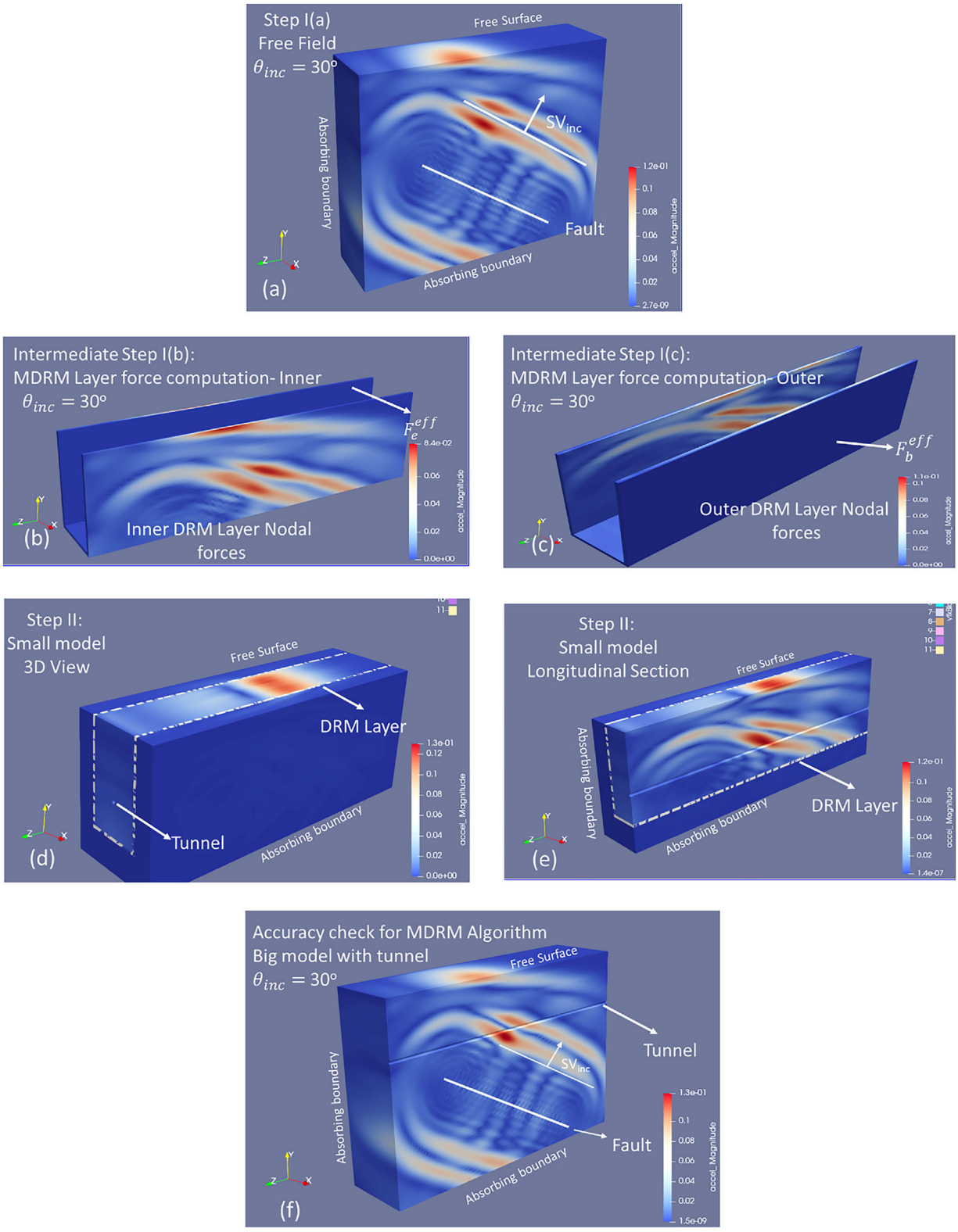


FIGURE 12 | MDRM numerical models: (a) Big model free field analysis with fault inclined at 30° (Step I(a)), (b) DRM inner layer nodal forces by fixing inner layer (Step I(b)), (c) DRM outer layer nodal forces by fixing outer layer (Step I(c)), (d) Small (reduced domain) model analysis using DRM forces–3D view, (e) Small (reduced domain) model analysis using DRM forces—sectional view, and (f) Large model analysis considering tunnel, fault rupture, and geological features in the domain.

10969853, 2025, 13, Downloaded from https://onlinelibrary.wiley.com/doi/10.1002/nag.70006 by The Librarian, Wiley Online Library on [14/08/2025]. See the Terms and Conditions (https://onlinelibrary.wiley.com/terms-and-conditions) on Wiley Online Library for rules of use; OA articles are governed by the applicable Creative Commons License

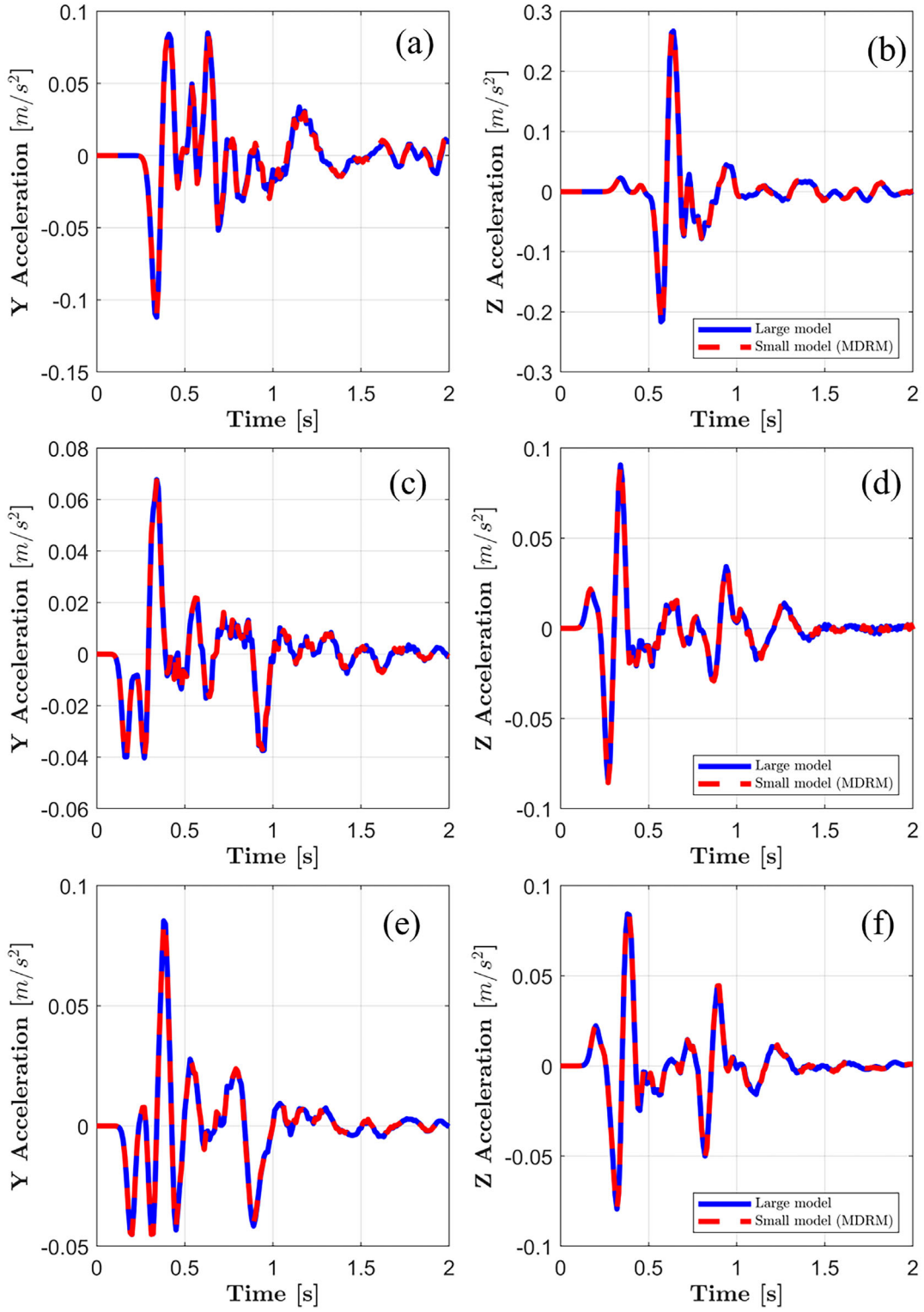


FIGURE 13 | Acceleration comparison at [X = 250 m, Y = 0 m and Z = 500 m], [X = 250 m, Y = 150 m and Z = 500 m], [X = 256 m, Y = 200 m and Z = 500 m], and (a, c, e) Y component, and (b, d, f) Z component acceleration respectively.

considered. Furthermore, the transfer function is compared with the approaches existing in literature, namely, Aki and Richards [15] and Kramer [17]. We observe good agreement among the transfer functions (see Figure 16). Figure 17 shows the transfer function of each layer to the bedrock and shows that the peak amplitude decays for the layers close to the bedrock, accompanied by increased *noise*.

4 | Results and Discussion

To demonstrate our proposed methodology MDRM, a 5-layer soil profile is considered, as shown in Figure 8, and the soil layer properties are tabulated in Table 2. We have performed a parametric analysis considering three tunnel sections, namely, circular (C), square (S), and horseshoe (H) sections

10969853, 2025, 13, Downloaded from https://onlinelibrary.wiley.com/doi/10.1002/nag.70006 by The Librarian, Wiley Online Library on [14/08/2025]. See the Terms and Conditions (https://onlinelibrary.wiley.com/terms-and-conditions) on Wiley Online Library for rules of use; OA articles are governed by the applicable Creative Commons License

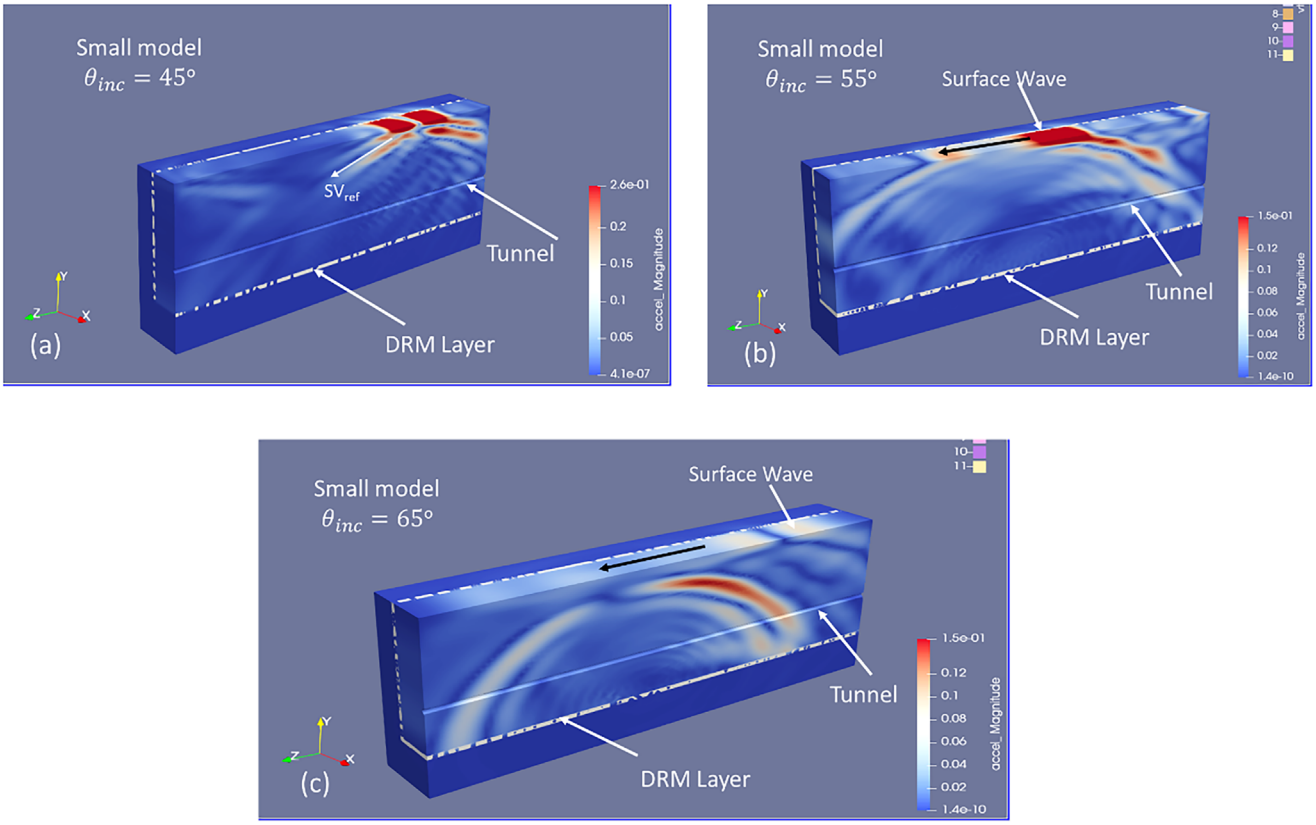


FIGURE 14 | Complex wave-structure interaction in the domain: (a) $\theta_{inc} = 45^{\circ}$, (b) $\theta_{inc} = 55^{\circ}$, and (c) $\theta_{inc} = 65^{\circ}$.

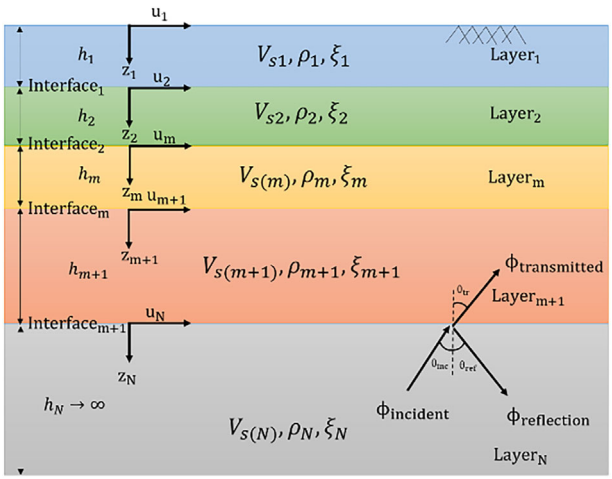


FIGURE 15 | Schematic of N-layer profile showing incidence, reflection, and transmission of shear wave.

(Figure 18a–c), and four fault inclination angles: 30°, 45°, 55°, and 65° (see Figure 11a–d). The tunnel dimensions were chosen to ensure identical areas for each section. This setup allows us to evaluate the influence of the inclination angle on the overall response of the tunnels.

We conducted each simulation over a time duration of 2.0 s such that seismic wave propagation, its interaction with the tunnel, and scattered waves attenuated from the domain (see Figure 14) are captured.

4.1 | Stress Variation of Different Tunnel Cross-Sections

The von Mises stress variation at $Z = 500$ m for C, S, and H cross sections at various time instants is shown in Figures 19, 20, and 21, respectively. For all the sections, peak von Mises stress (pVM):

$$pVM\ (t) = \max_{x \in \Omega} \sigma_{vM}\,(x, t) \tag{17}$$

is observed at $\theta = 0^{\circ}, 180^{\circ}$ at different time step t. This is because the incident waves emanating from the source of excitation interact with the tunnel surface. At the tunnel-surface interface, the waves undergo scattering and transmission. Once the waves leave the interface, there is a decrease in von Mises stress. The transmitted waves, upon reflection at the free surface, interact with the tunnel again, leading to an increase in von Mises stress at $t = 0.80$ s for all sections. However, due to damping, the wave intensity reduces.

In the analysis of the C section in layer 4, the pVM is consistently observed across all temporal variations at the 0° and 180° locations. At $t = 0.30$ s, the stress increases with the dip angle until it reaches 45°, after which it decreases for higher dip angles, continuing this trend until $t = 0.60$ s. By $t = 0.80$ s, a shift in stress dominance occurs at a 65° inclination angle, primarily due to the contribution of reflected seismic waves, which become increasingly significant at this stage. Throughout, the von Mises stresses at the 90° and 270° locations remain minimal, irrespective of the temporal and spatial variations of the seismic waves. Similarly, for the S section in layer 4, the von

10969853, 2025, 13, Downloaded from https://onlinelibrary.wiley.com/doi/10.1002/nag.70006 by The Librarian, Wiley Online Library on [14/08/2025]. See the Terms and Conditions (https://onlinelibrary.wiley.com/terms-and-conditions) on Wiley Online Library for rules of use; OA articles are governed by the applicable Creative Commons License

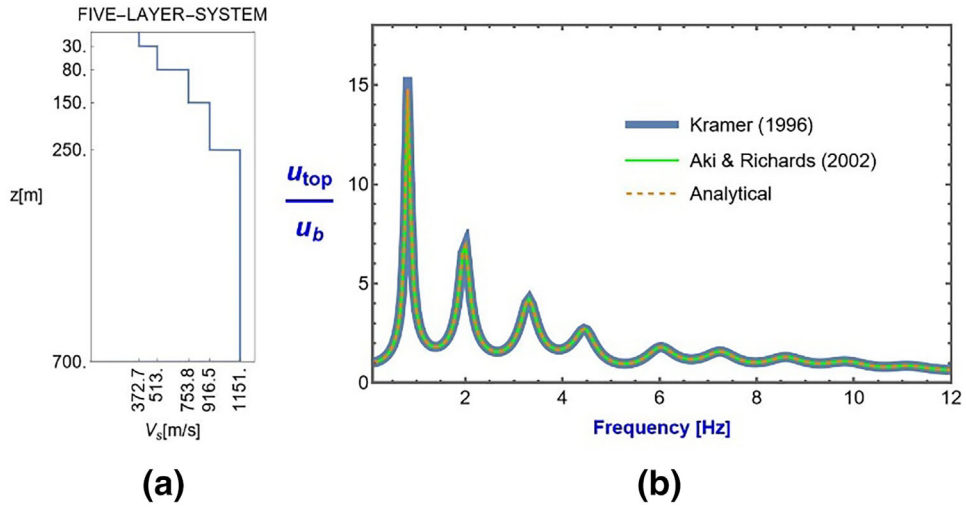


FIGURE 16 | (a) Variation of shear wave velocity with depth for 5-layer profile, (b) Comparison of transfer functions obtained by different approaches.

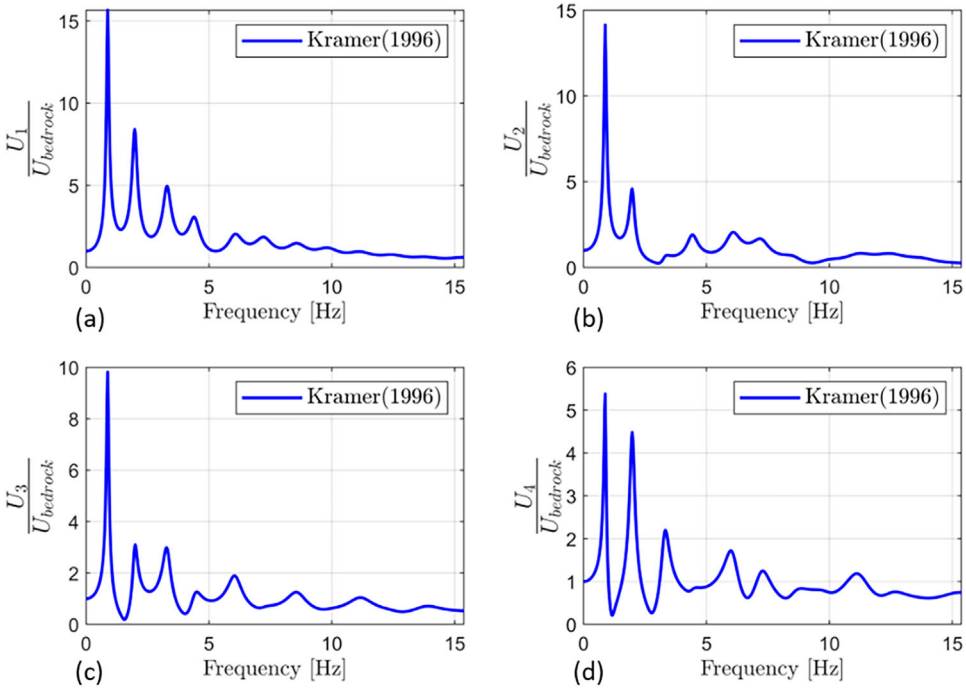


FIGURE 17 | Transfer function for each layer with respect to bedrock: (a) Layer 1, (b) Layer 2, (c) Layer 3, and (d) Layer 4.

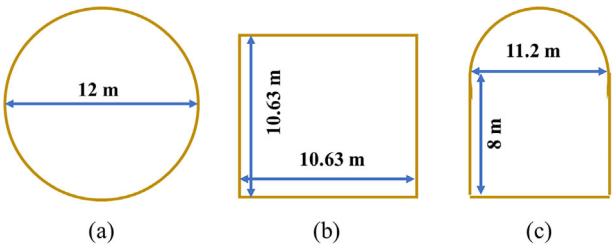


FIGURE 18 | Different tunnel sections considered for analysis: (a) Circular, (b) Square, and (c) Horseshoe sections.

Mises stress initially increases with the inclination angle up to 45° but decreases beyond this angle at early time steps. As time progresses, the stress response intensifies at higher inclination angles. The stress distribution around the tunnel aligns with the S section's lateral faces, showing uniformity in the lateral direction, while the top and bottom areas display non-uniform variation. Corner singularities in the S section play a crucial role in the overall stress distribution.

For the H section in layer 4, the stress distribution exhibits minimum von Mises stresses at the 90° and 270° locations. At $t = 0.60$ s, the stress increases with the inclination angle, peaking at 45°, but decreases with higher inclination angles as time progresses, a trend influenced by the contribution of reflected waves. Notably, the stresses at the corners of the H section decrease significantly, and the overall stress variation follows a

10969853, 2025, 13, Downloaded from https://onlinelibrary.wiley.com/doi/10.1002/nag.70006 by The Librarian, Wiley Online Library on [14/08/2025]. See the Terms and Conditions (https://onlinelibrary.wiley.com/terms-and-conditions) on Wiley Online Library for rules of use; OA articles are governed by the applicable Creative Commons License

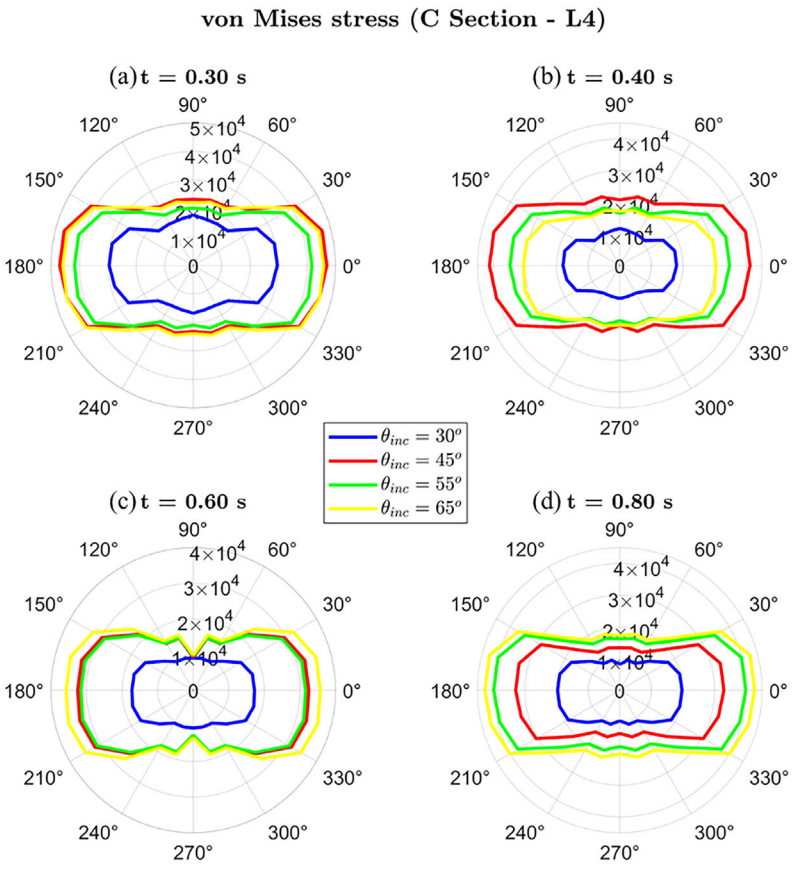


FIGURE 19 | von Mises stress variation for circular section located in layer 4.

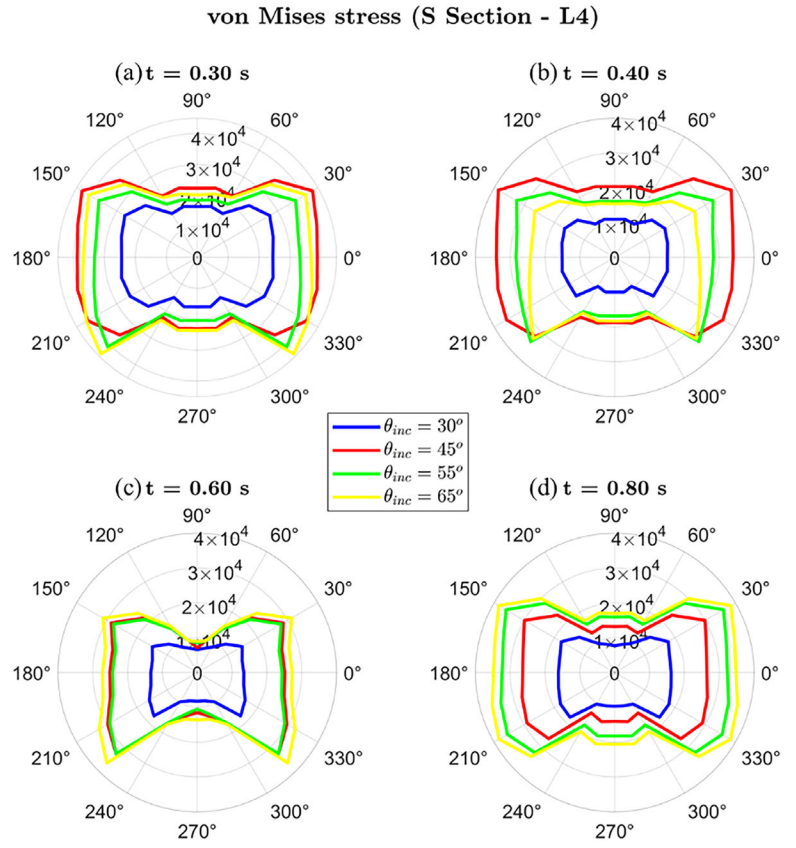


FIGURE 20 | von Mises stress variation for square section located in layer 4.

10969853, 2025, 13, Downloaded from https://onlinelibrary.wiley.com/doi/10.1002/nag.70006 by The Librarian, Wiley Online Library on [14/08/2025]. See the Terms and Conditions (https://onlinelibrary.wiley.com/terms-and-conditions) on Wiley Online Library for rules of use; OA articles are governed by the applicable Creative Commons License

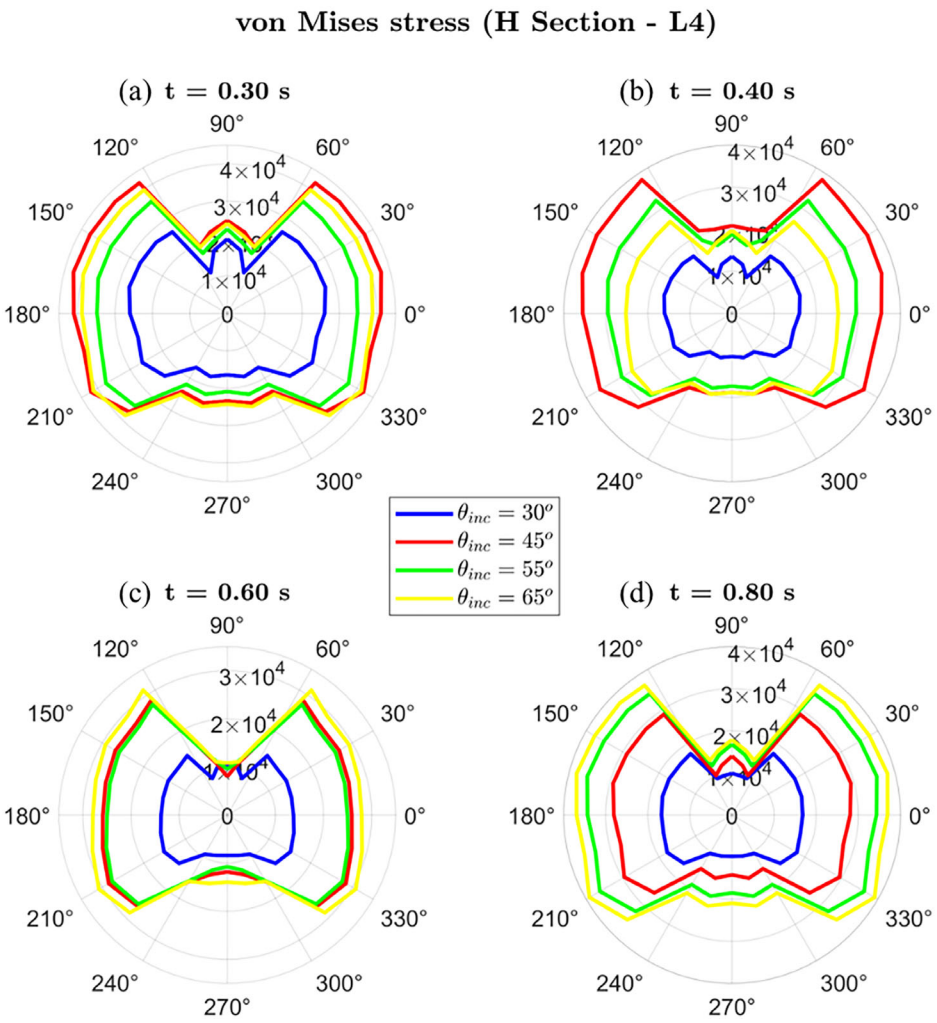


FIGURE 21 | von Mises stress variation for horseshoe section located in layer 4.

near-quadratic pattern. Among the considered sections, the H section demonstrates the lowest von Mises stress values, making it the most economical and efficient design for ensuring safety. Its ability to minimize stress concentrations, especially under seismic loading conditions, positions it as the most structurally efficient option compared to C and S sections.

4.2 | Layer-Wise Variation for Circular Cross-Section

We conducted a comparative analysis of the stresses in layers 2 (see Figures 22(a, b), and 23), and 3 (see Figures 22(c, d) and 24) for the C section. Lower values of von Mises stress were observed at 90° and 270°. The von Mises stress initially exhibited two lobes at lower time steps, which eventually morphed into a single lobe at higher time steps. In layer 4, the initial response was dominated by the 45° inclination, whereas in layer 2, the 65° inclination angle governed the maximum response. However, for later time steps in layer 2, the 45° dip angle produced the highest response, as the reflected wave interacting with the tunnel had the same energy as the incident wave (see Table 3).

For the C section in layer 3, the response initially increased with the inclination angle, reaching a maximum at 45°, after which it decreased. The maximum stress was observed at higher time steps for larger inclination angles. Overall, the stress values in layer 2 were lower than those in layers 3 and 4. The observed seismic response can be primarily attributed to the proximity of layers 3 and 4 to the seismic source and the interface between geological layers. In this context, the characteristics of seismic wave propagation are significantly influenced by the interaction of waves with these layers. As seismic waves travel through the subsurface, they encounter varying material properties at layer boundaries, leading to multiple reflections and refractions. These interactions result in complex wave behavior, with waves reflecting back into deeper layers and refracting at angles that vary according to the material's acoustic impedance.

As waves propagate upward through these layers, transmitted waves tends to bend closer to the normal direction relative to the surface. This phenomenon occurs due to the principles of wave refraction, which dictate that waves slow down in less dense materials. Additionally, the upward propagation of waves is subject to attenuation mechanisms, such as radiation damping, which diminish wave amplitude and energy as they traverse through layers. Consequently, layer 2 exhibits a reduced impact from seismic waves due to its intermediate position and the cumulative effects of reflection and refraction occurring

10969853, 2025, 13, Downloaded from https://onlinelibrary.wiley.com/doi/10.1002/nag.70006 by The Librarian, Wiley Online Library on [14/08/2025]. See the Terms and Conditions (https://onlinelibrary.wiley.com/terms-and-conditions) on Wiley Online Library for rules of use; OA articles are governed by the applicable Creative Commons License

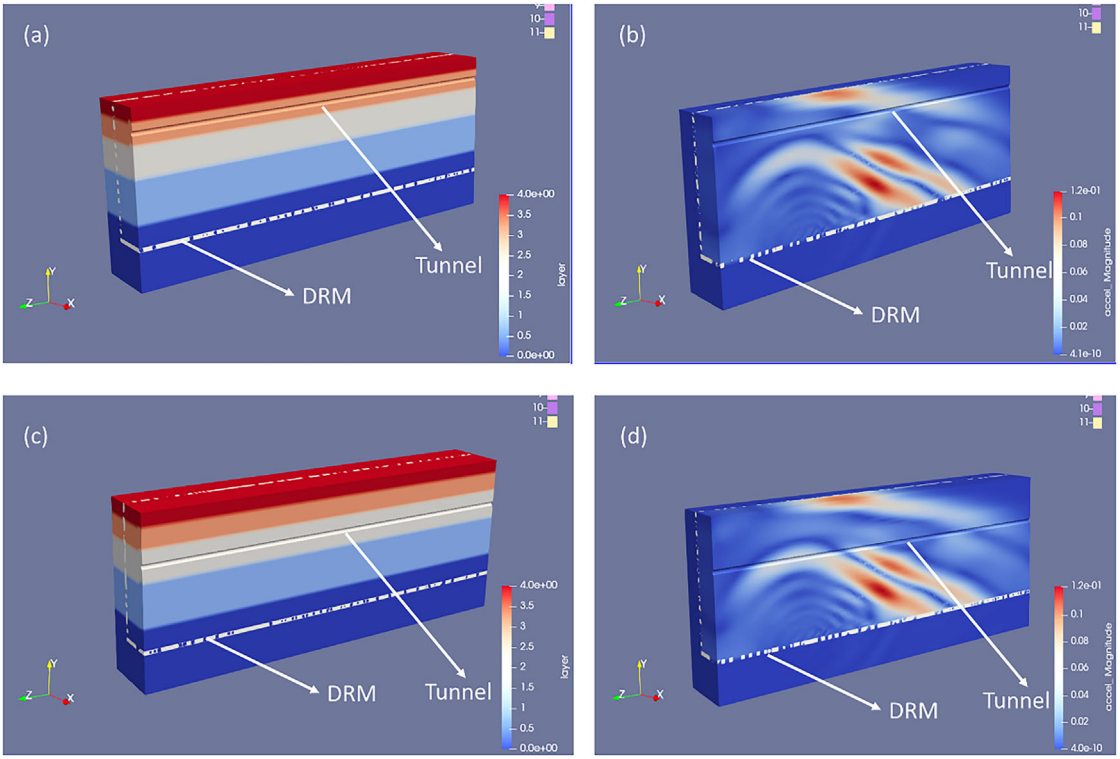


FIGURE 22 | (a, b) Tunnel located in the second layer and corresponding wave dynamics, and (c, d) Tunnel located in the third layer and corresponding wave dynamics.

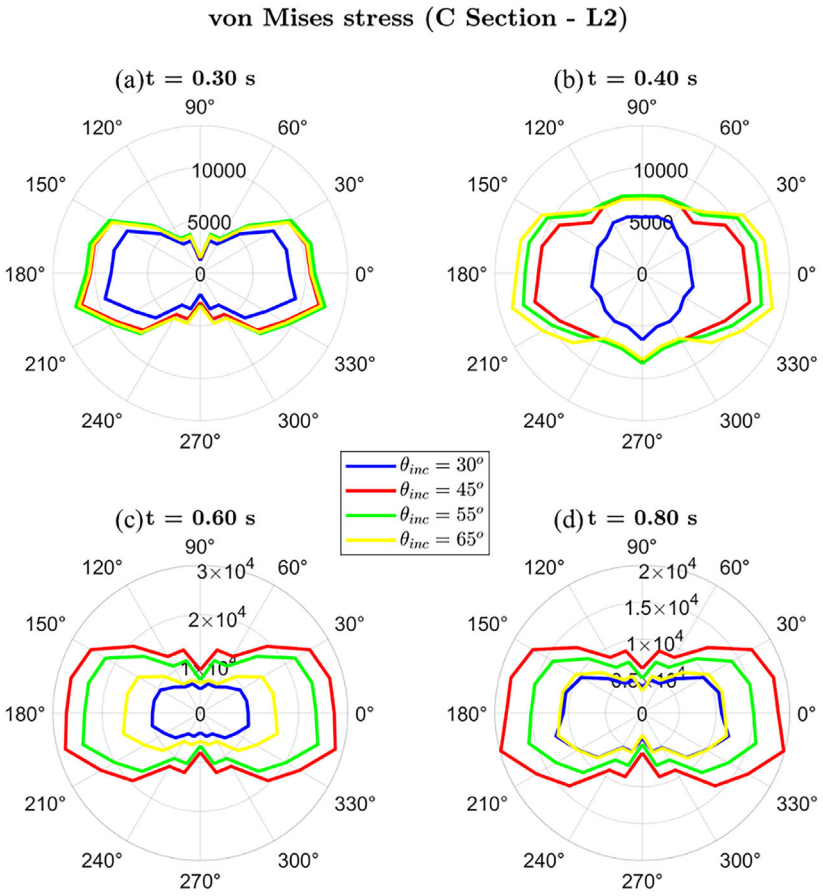


FIGURE 23 | von Mises stress variation for a circular section located in layer 2.

10969853, 2025, 13, Downloaded from https://onlinelibrary.wiley.com/doi/10.1002/nag.70006 by The Librarian, Wiley Online Library on [14/08/2025]. See the Terms and Conditions (https://onlinelibrary.wiley.com/terms-and-conditions) on Wiley Online Library for rules of use; OA articles are governed by the applicable Creative Commons License

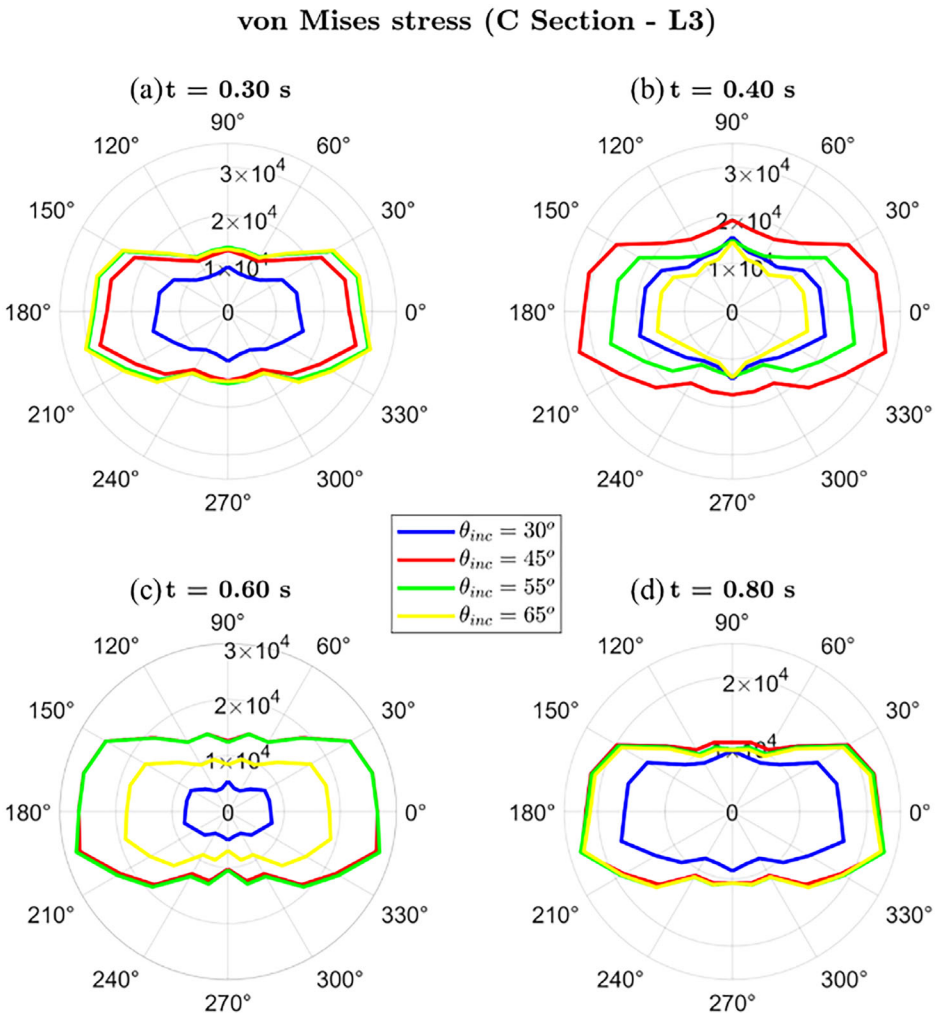


FIGURE 24 | von Mises stress variation for circular section located in layer 3.

primarily in the adjacent layers. This attenuation underscores the importance of understanding subsurface layering for accurate seismic analysis and interpretation.

5 | Conclusions

This paper presents a novel and robust multi-layer modified DRM algorithm for modeling the complex wave fields in the layered soil media. It also addresses the intricate task of modeling complex fault ruptures and their impacts on tunnels in stratified geological environments. To illustrate our proposed methodology, a 5-layer soil profile was considered, including the inclined seismic fault and the tunnel. Three canonical tunnel cross-sections, namely, circular, square, and horseshoe were selected, and their response to seismic waves was analyzed across four fault inclination angles: 30°, 45°, 55°, and 65°. These varied configurations allowed a comprehensive assessment of the influence of tunnel shape and fault orientation on seismic resilience.

To evaluate the seismic responses, von Mises stress plots were generated, revealing that the horseshoe-shaped tunnel demonstrated superior efficiency in withstanding seismic impacts. The locations of the tunnels have been varied to assess how depth influences seismic behavior, providing qualitative insights into optimal placement strategies for such underground structures.

The dynamic response of the tunnel was analyzed under different transfer function determination techniques available in the literature. This approach facilitated a detailed understanding of seismic wave propagation through the layered media and its interaction with the tunnel structure. The MDRM algorithm was implemented in a MOOSE-based open-source finite element package MASTODON, enabling the precise simulation of the complex seismic scenarios considered in this study.

These research findings underscore the effectiveness of the MDRM algorithm in capturing the intricate details of seismic wave fields and fault rupture dynamics. The study provides a robust framework for designing tunnels in seismically active regions by verifying this approach with various tunnel geometries and inclination angles. The results highlight the horseshoe tunnel's superior performance, especially in stress distribution, and offer crucial insights into the influence of tunnel depth on seismic resilience. This comprehensive analysis will serve as a guide for developing engineered materials to mitigate the impact of seismic waves on critical structures and facilities. This study can be extended by incorporating nonlinear effects, such as interface friction laws, lining degradation, and localized soil nonlinearity,

10969853, 2025, 13, Downloaded from https://onlinelibrary.wiley.com/doi/10.1002/nag.70006 by The Librarian, Wiley Online Library on [14/08/2025]. See the Terms and Conditions (https://onlinelibrary.wiley.com/terms-and-conditions) on Wiley Online Library for rules of use; OA articles are governed by the applicable Creative Commons License

which are crucial for fragility analysis and performance-based design of tunnels.

Author Contributions

Bhavesh Banjare: conceptualization, methodology, software, data curation, result analysis, writing – original draft. **Gauri Ranjan Krishna Chand Avatar:** conceptualization, methodology, result analysis, writing – review and editing. **Goudappa Ramanagouda Dodagoudar:** methodology, supervision, writing – review and editing.

Acknowledgments

The authors sincerely acknowledge the support provided by the MoE (Ministry of Education, Govt. of India) scholarship for post-graduate researchers.

Conflicts of Interest

The authors declare no conflicts of interest.

Data Availability Statement

Data will be made available on request.

References

1. Y. Jiang, C. Wang, and X. Zhao, "Damage Assessment of Tunnels Caused by the 2004 Mid Niigata Prefecture Earthquake Using Hayashi's Quantification Theory Type II," *Natural Hazards* 53 (2010): 425–441, https://doi.org/10.1007/S11069-009-9441-9.

2. H. Yu, J. Chen, A. Bobet, and Y. Yuan, "Damage Observation and Assessment of the Longxi Tunnel During the Wenchuan Earthquake," *Tunnelling and Underground Space Technology* 54 (2016): 102–116, https://doi.org/10.1016/J.TUST.2016.02.008.

3. J. Lai, S. He, J. Qiu, et al., "Characteristics of Seismic Disasters and Aseismic Measures of Tunnels in Wenchuan Earthquake," *Environmental Earth Sciences* 76 (2017): 1–19, https://doi.org/10.1007/S12665-017-6405-3.

4. W. L. Wang, T. T. Wang, J. J. Su, C. H. Lin, C. R. Seng, and T. H. Huang, "Assessment of Damage in Mountain Tunnels due to the Taiwan Chi-Chi Earthquake," *Tunnelling and Underground Space Technology* 16 (2001): 133–150, https://doi.org/10.1016/S0886-7798(01)00047-5.

5. Z. Chen, C. Shi, T. Li, and Y. Yuan, "Damage Characteristics and Influence Factors of Mountain Tunnels Under Strong Earthquakes," *Natural Hazards* 61 (2012): 387–401, https://doi.org/10.1007/S11069-011-9924-3.

6. Y. Shen, B. Gao, X. Yang, and S. Tao, "Seismic Damage Mechanism and Dynamic Deformation Characteristic Analysis of Mountain Tunnel After Wenchuan Earthquake," *Engineering Geology* 180 (2014): 85–98, https://doi.org/10.1016/J.ENGGEO.2014.07.017.

7. X. Zhang, Y. Jiang, and S. Sugimoto, "Seismic Damage Assessment of Mountain Tunnel: A Case Study on the Tawarayama Tunnel due to the 2016 Kumamoto Earthquake," *Tunnelling and Underground Space Technology* 71 (2018): 138–148, https://doi.org/10.1016/J.TUST.2017.07.019.

8. G. N. Owen and R. E. Scholl, Division U. S. F. H. A. S. and AM, Foundation NS. Earthquake engineering of large underground structures. 1981, https://rosap.ntl.bts.gov/view/dot/30095.

9. M. Corigliano, L. Scandella, C. G. Lai, and R. Paolucci, "Seismic Analysis of Deep Tunnels in near Fault Conditions: A Case Study in Southern Italy," *Bulletin of Earthquake Engineering* 9 (2011): 975–995, https://doi.org/10.1007/S10518-011-9249-3.

10. G. Wu, H. Zhao, M. Zhao, and Z. Zhu, "Stochastic Analysis of Dual Tunnels in Spatially Random Soil," *Computers and Geotechnics* 129 (2021): 103861, https://doi.org/10.1016/J.COMPGEO.2020.103861.

11. B. Banjare and G. Avatar, "Stochastic Assessment of 3-D Tunnels in Near-Fault Ground Motion Using Modified Domain Reduction Method," *International Journal for Numerical and Analytical Methods in Geomechanics* 48 (2024): 2259–2284, https://doi.org/10.1002/NAG.3733.

12. J. Garcia-Suarez, J. González-Carbajal, and D. Asimaki, "Analytical 1D Transfer Functions for Layered Soils," *Soil Dynamics and Earthquake Engineering* 163 (2022): 107532, https://doi.org/10.1016/J.SOILDYN.2022.107532.

13. J. Garcia-Suarez, "Harmonic Decomposition of the Trace of 1D Transfer Matrices in Layered Media," *Journal of the Mechanics and Physics of Solids* 163 (2022): 104830, https://doi.org/10.1016/J.JMPS.2022.104830.

14. F. Gilbert and G. E. Backus, "Propagator Matrices in Elastic Wave and Vibration Problems," *Geophysics* 31 (2012): 326–332, https://doi.org/10.1190/1.1439771.

15. K. Aki and P. G. Richards, *Quantitative Seismology* (University Science Books, 2002).

16. A. Ben-Menahem and S. J. Singh, *Seismic Waves and Sources* (1981), https://doi.org/10.1007/978-1-4612-5856-8.

17. S. L. Kramer, *Geotechnical Earthquake Engineering* (Prentice Hall, 1996).

18. H. Z. Jahromi, B. A. Izzuddin, and L. Zdravkovic, "A Domain Decomposition Approach for Coupled Modelling of Nonlinear Soil–Structure Interaction," *Computer Methods in Applied Mechanics and Engineering* 198 (2009): 2738–2749, https://doi.org/10.1016/J.CMA.2009.03.018.

19. J. Chen, B. Zhu, W. Zhong, and Q. H. Liu, "A Semianalytical Spectral Element Method for the Analysis of 3-D Layered Structures," *IEEE Transactions on Microwave Theory and Techniques* 59 (2011): 1–8, https://doi.org/10.1109/TMTT.2010.2090408.

20. J. Chen, "A Semianalytical Finite Element Analysis of Electromagnetic Propagation in Stratified media," *Microwave and Optical Technology Letters* 57 (2015): 15–18, https://doi.org/10.1002/MOP.28786.

21. J. Chen, "An Efficient Layered Finite Element Method With Domain Decomposition for Simulations of Resistivity Well Logging," *Journal of Petroleum Science & Engineering* 150 (2017): 217–223, https://doi.org/10.1016/J.PETROL.2016.11.039.

22. M. S. Ozer, H. Koruk, and K. Y. Sanliturk, "Development of an Equivalent Shell Finite Element for Modelling Damped Multi-Layered Composite Structures," *Composite Structures* 254 (2020): 112828, https://doi.org/10.1016/J.COMPSTRUCT.2020.112828.

23. J. Zhao, P. K. Wong, X. Ma, Z. Xie, J. Xu, and V. A. Cristino, "Simplification of Finite Element Modeling for Plates Structures With Constrained Layer Damping by Using Single-Layer Equivalent Material Properties," *Composites Part B: Engineering* 157 (2019): 283–288, https://doi.org/10.1016/J.COMPOSITESB.2018.09.010.

24. T. L. Teng and N. K. Hu, "Analysis of Damping Characteristics for Viscoelastic Laminated Beams," *Computer Methods in Applied Mechanics and Engineering* 190 (2001): 3881–3892, https://doi.org/10.1016/S0045-7825(00)00305-4.

25. P. Li and E. X. Song, "Three-Dimensional Numerical Analysis for the Longitudinal Seismic Response of Tunnels Under an Asynchronous Wave Input," *Computers and Geotechnics* 63 (2015): 229–243, https://doi.org/10.1016/J.COMPGEO.2014.10.003.

26. J. Q. Huang, X. L. Du, L. Jin, and M. Zhao, "Impact of Incident Angles of P Waves on the Dynamic Responses of Long Lined Tunnels," *Earthquake Engineering & Structural Dynamics* 45 (2016): 2435–2454, https://doi.org/10.1002/EQE.2772.

27. J. Huang, M. Zhao, and X. Du, "Non-Linear Seismic Responses of Tunnels Within Normal Fault Ground Under Obliquely Incident P Waves," *Tunnelling and Underground Space Technology* 61 (2017): 26–39, https://doi.org/10.1016/J.TUST.2016.09.006.

28. S. Argyroudis, G. Tsinidis, F. Gatti, and K. Pitilakis, "Effects of SSI and Lining Corrosion on the Seismic Vulnerability of Shallow Circular

10969853, 2025, 13, Downloaded from https://onlinelibrary.wiley.com/doi/10.1002/nag.70006 by The Librarian, Wiley Online Library on [14/08/2025]. See the Terms and Conditions (https://onlinelibrary.wiley.com/terms-and-conditions) on Wiley Online Library for rules of use; OA articles are governed by the applicable Creative Commons License

Tunnels," *Soil Dynamics and Earthquake Engineering* 98 (2017): 244–256, https://doi.org/10.1016/J.SOILDYN.2017.04.016.

29. H. Wang, H. Yang, Y. Feng, and B. Jeremić, "Modeling and Simulation of Earthquake Soil Structure Interaction Excited by Inclined Seismic Waves," *Soil Dynamics and Earthquake Engineering* 146 (2021): 106720, https://doi.org/10.1016/J.SOILDYN.2021.106720.

30. M. Korres, F. Lopez-Caballero, V. Alves Fernandes, F. Gatti, I. Zentner, and F. Voldoire, "Enhanced Seismic Response Prediction of Critical Structures via 3D Regional Scale Physics-Based Earthquake Simulation," *Journal of Earthquake Engineering* 27 (2023): 546–574, https://doi.org/10.1080/13632469.2021.2009061.

31. W. Zhang, E. E. Seylabi, and E. Taciroglu, "An ABAQUS Toolbox for Soil-Structure Interaction Analysis," *Computers and Geotechnics* 114 (2019): 103143, https://doi.org/10.1016/J.COMPGEO.2019.103143.

32. W. Zhang and E. Taciroglu, "3D Time-Domain Nonlinear Analysis of Soil-Structure Systems Subjected to Obliquely Incident SV Waves in Layered Soil Media," *Earthquake Engineering & Structural Dynamics* 50 (2021): 2156–2173, https://doi.org/10.1002/EQE.3443.

33. B. Banjare and S. Veeraraghavan, "Seismic Assessment of Tunnels in Near Fault Ground Motion," *Proceedings of 17th Symposium on Earthquake Engineering* 3 (2023): 185–197, https://doi.org/10.1007/978-981-99-1579-8_15.

34. B. Banjare, "Seismic Evaluation of 3D Tunnels in Near Fault Ground Motion Using Domain Reduction Method" (master's thesis, Indian Institute of Science, 2023), https://etd.iisc.ac.in/handle/2005/6328.

35. S. Veeraraghavan and B. Banjare, "A Modified Domain Reduction Method for Analysing the 3D Seismic Response of Long Tunnels," *Tunnelling and Underground Space Technology* 159 (2025): 106461, https://doi.org/10.1016/J.TUST.2025.106461.

36. W. B. Joyner and A. T. F. Chen, "Calculation of Nonlinear Ground Response in Earthquakes," *Bulletin of the Seismological Society of America* 65 (1975): 1315–1336, https://doi.org/10.1785/BSSA0650051315.

37. J. Lysmer, "Analytical Procedures in Soil Dynamics," *ASCE Geotechnical Engineering Division Specialty Conference on Earthquake Engineering and Soil Dynamics* 80 (1978): 12243.

38. J. Lysmer and R. L. Kuhlemeyer, "Finite Dynamic Model for Infinite Media," *Journal of the Engineering Mechanics Division* 95 (1969): 859–877, https://doi.org/10.1061/JMCEA3.0001144.

39. L. Jingbo and L. Yandong, "A Direct Method for Analysis of Dynamic Soil-Structure Interaction Based on Interface Idea," *Developments in Geotechnical Engineering* 83 (1998): 261–276, https://doi.org/10.1016/S0165-1250(98)80018-7.

40. P. R. Saastamoinen, "On Propagators and Scatterers in Wave Problems of Layered, Elastic Media—A Spectral Approach," *Bulletin of the Seismological Society of America* 70 (1980): 1125–1135, https://doi.org/10.1785/BSSA0700041125.

41. E. Kausel and J. M. Roësset, "Stiffness Matrices for Layered Soils," *Bulletin of the Seismological Society of America* 71 (1981): 1743–1761, https://doi.org/10.1785/BSSA0710061743.

42. N. A. Haskell, "The Dispersion of Surface Waves on Multilayered Media," in *Vincit Veritas: A Portrait of the Life and Work of Norman Abraham Haskell, 1905–1970* (American Geophysical Union, 2011), 86–103, https://doi.org/10.1029/SP030P0086.

43. W. T. Thomson, "Transmission of Elastic Waves Through a Stratified Solid Medium," *Journal of Applied Physics* 21 (1950): 89–93, https://doi.org/10.1063/1.1699629.

44. E. Kausel, "Thin-Layer Method: Formulation in the Time Domain," *International Journal for Numerical Methods in Engineering* 37 (1994): 927–941, https://doi.org/10.1002/NME.1620370604.

45. R. Shen, H. Waisman, and L. Guo, "Fracture of Viscoelastic Solids Modeled With a Modified Phase Field Method," *Computer Methods in Applied Mechanics and Engineering* 346 (2019): 862–890, https://doi.org/10.1016/J.CMA.2018.09.018.

46. J. Bielak, K. Loukakis, Y. Hisada, and C. Yoshimura, "Domain Reduction Method for Three-Dimensional Earthquake Modeling in Localized Regions, Part I: Theory," *Bulletin of the Seismological Society of America* 93 (2003): 817–824, https://doi.org/10.1785/0120010251.

47. C. Yoshimura, J. Bielak, Y. Hisada, and A. Fernández, "Domain Reduction Method for Three-Dimensional Earthquake Modeling in Localized Regions, Part II: Verification and Applications," *Bulletin of the Seismological Society of America* 93 (2003): 825–841, https://doi.org/10.1785/0120010252.

48. S. Kontoe, L. Zdravkovic, and D. Potts, "The Domain Reduction Method for Dynamic Coupled Consolidation Problems in Geotechnical Engineering," *International Journal for Numerical and Analytical Methods in Geomechanics* 32 (2008): 659–680, https://doi.org/10.1002/NAG.641.

49. S. Kontoe, L. Zdravkovic, and D. M. Potts, "An Assessment of the Domain Reduction Method as an Advanced Boundary Condition and some Pitfalls in the Use of Conventional Absorbing Boundaries," *International Journal for Numerical and Analytical Methods in Geomechanics* 33 (2009): 309–330, https://doi.org/10.1002/nag.713.

50. M. Tao, H. T. Zhao, Z. W. Li, and J. B. Zhu, "Analytical and Numerical Study of a Circular Cavity Subjected to Plane and Cylindrical P-wave Scattering," *Tunnelling and Underground Space Technology* 95 (2020): 103143, https://doi.org/10.1016/J.TUST.2019.103143.

51. V. W. Lee and J. Karl, "Diffraction of SV Waves by Underground, Circular, Cylindrical Cavities," *Soil Dynamics and Earthquake Engineering* 11 (1992): 445–456, https://doi.org/10.1016/0267-7261(92)90008-2.

52. H. Liu and E. Song, "Seismic Response of Large Underground Structures in Liquefiable Soils Subjected to Horizontal and Vertical Earthquake Excitations," *Computers and Geotechnics* 32 (2005): 223–244, https://doi.org/10.1016/J.COMPGEO.2005.02.002.

53. A. Amorosi and D. Boldini, "Numerical Modelling of the Transverse Dynamic Behaviour of Circular Tunnels in Clayey Soils," *Soil Dynamics and Earthquake Engineering* 29 (2009): 1059–1072, https://doi.org/10.1016/J.SOILDYN.2008.12.004.

54. S. Veeraraghavan, "Semi-Analytical Solution for the 3D Response of Tunnels Subjected to Seismic Waves," *Tunnelling and Underground Space Technology* 152 (2024): 105925, https://doi.org/10.1016/J.TUST.2024.105925.

55. J. Coleman, A. Slaughter, S. Veeraraghavan, et al., *MASTODON Theory Manual* (Idaho National Laboratory, 2017), https://doi.org/10.2172/1376857.

56. S. Veeraraghavan, J. L. Coleman, and J. Bielak, "Simulation of Site and Topographic Effects on Ground Motion in Los Alamos, NM Mesas," *Geophysical Journal International* 220 (2020): 1504–1520, https://doi.org/10.1093/GJI/GGZ448.

57. F. Ihlenburg and I. Babuška, "Finite Element Solution of the Helmholtz Equation With High Wave Number Part I: The h-version of the FEM," *Computers & Mathematics With Applications* 30 (1995): 9–37, https://doi.org/10.1016/0898-1221(95)00144-N.

58. N. M. Newmark, "A Method of Computation for Structural Dynamics," *Journal of the Engineering Mechanics Division* 85 (1959): 67–94, https://doi.org/10.1061/JMCEA3.0000098.

59. B. R. Ahrabi and D. J. Mavriplis, "An Implicit Block ILU Smoother for Preconditioning of Newton–Krylov Solvers With Application in High-Order Stabilized Finite-Element Methods," *Computer Methods in Applied Mechanics and Engineering* 358 (2020): 112637, https://doi.org/10.1016/J.CMA.2019.112637.

60. F. Pisanò and M. Pastor, "1D wave Propagation in Saturated Viscous Geomaterials: Improvement and Validation of a Fractional Step Taylor–Galerkin Finite Element Algorithm," *Computer Methods in Applied Mechanics and Engineering* 200 (2011): 3341–3357, https://doi.org/10.1016/J.CMA.2011.07.011.

61. L. Evans, *Partial Differential Equations* (American Mathematical Society, 2022).

10969853, 2025, 13, Downloaded from https://onlinelibrary.wiley.com/doi/10.1002/nag.70006 by The Librarian, Wiley Online Library on [14/08/2025]. See the Terms and Conditions (https://onlinelibrary.wiley.com/terms-and-conditions) on Wiley Online Library for rules of use; OA articles are governed by the applicable Creative Commons License